1
Surface Electrochemistry with Pt Single-Crystal Electrodes

Victor Climent and Juan M. Feliu

1.1
Introduction

The sensitivity of electrochemical processes to the crystallographic structure of the electrode surface is now a well-established fact demonstrated for numerous reactions. Except for outer sphere processes, the majority of electrochemical reactions involve the formation of adsorbed intermediates. In fact, the concepts underneath the electrocatalytic phenomena are intimately linked to the existence of strong interactions of reacting species and the electrode surface [1]. In this case, adsorption energies are very sensitive to the geometries of the adsorption sites, strongly affecting the energetic pathway from reactants to products and, in consequence, the rate of the reaction.

In addition, the properties of the interphase are affected by the crystallographic structure of the electrode. Considering that the electron transfer has to take place in the narrow region that separates the metal from the solution, it is easy to understand that the interfacial properties will also have strong effect on the rate of most reactions. Anion-specific adsorption, distribution of charges at the interphase, and even interaction of water with the metal surface are aspects of the interphase that need to be considered in order to get the complete picture about the influence of the structure on the electrochemical reactivity.

In this sense, the approach of interfacial electrochemistry has been proved as very convenient (and inexpensive) to study the interaction of molecules and ions with metal surfaces. An iconic moment in the development of electrochemistry as a surface-sensitive approach is the introduction of the flame annealing methodology by the French scientist Jean Clavilier [2, 3]. Earlier attempts to obtain a surface-sensitive electrochemical response with well-defined metal surfaces resulted in dissimilar and contradictory results [4–8]. The flame annealing technique not only offered a much simpler method in comparison with the more complex approaches based on ultrahigh-vacuum (UHV) preparation of the surface but also offered the opportunity to perform the experiments in many different laboratories across the world, soon proving the reproducibility of the

Nanopatterned and Nanoparticle-Modified Electrodes, First Edition.
Edited by Richard C. Alkire, Philip N. Bartlett and Jacek Lipkowski.
© 2017 Wiley-VCH Verlag GmbH & Co. KGaA. Published 2017 by Wiley-VCH Verlag GmbH & Co. KGaA.

COPYRIGHTED MATERIAL

results. Immediately after the introduction of this methodology, some controversy arose because it revealed aspects of the electrochemical behavior of platinum not previously reported (the so-called unusual adsorption states) [9–11]. This initial controversy was soon resolved, and now the correct electrochemistry of platinum single crystals is well established and understood [11, 12].

The knowledge gained about the electrochemical reactivity of platinum from the studies using well-defined electrode surfaces has resulted in very useful understanding of the behavior of more complex electrode structures, such as polycrystalline materials and nanoparticles.

1.2 Concepts of Surface Crystallography

An atomically flat surface is generated by cutting a single crystal in a desired orientation with respect to the crystallographic axis of the crystal. The ideal surface that is obtained by such process can be understood as the result of removing all the atoms whose center lies on one side of the cutting plane and keeping all the atoms lying on the other side. Because the cutting plane does not necessarily pass through the center of all of the atoms, the resulting surface is not perfectly flat, and, in the more general case, the atomic centers of the atoms will define a regular distribution of terraces separated with steps which may also contain some corners or kinks. This process is illustrated in Figure 1.1 for the two-dimensional (2D) situation.

Each of these surfaces is designated with a set of three numbers (four for crystal in the hexagonal close-packed system) called *Miller indices* [13–15]. Miller indices are three integer numbers proportional to the reciprocal of the intersections of the mathematical plane used for defining the surface with the crystallographic axis of the crystal. This is illustrated in Figure 1.2.

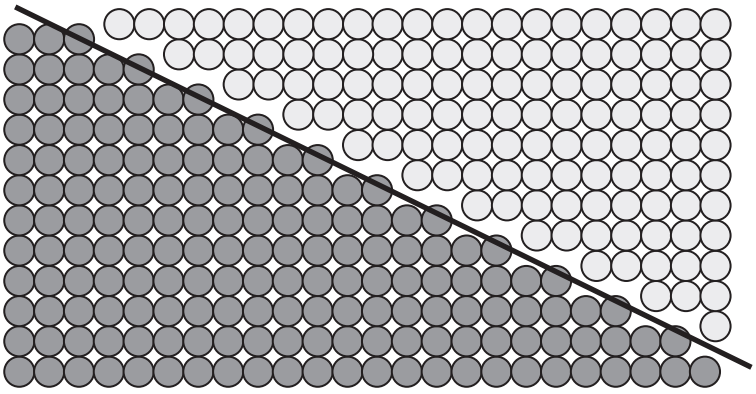

Figure 1.1 2D representation of the process of cutting a crystal through a plane, resulting on a stepped surface.

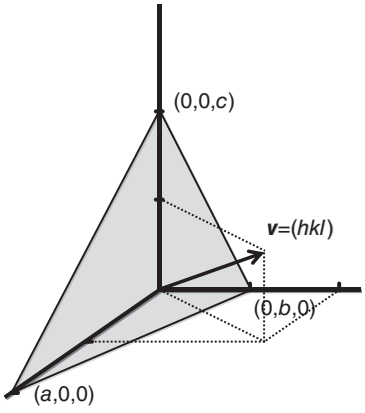

Figure 1.2 Illustration showing the definition of Miller indices of a surface as three integer numbers proportional to the reciprocal of the intercepts of the plane defining the surface with the three crystallographic axes.

For cubic crystals, Miller indices define a vector that is perpendicular to the surface. This is very convenient, since it allows using vector calculus to easily obtain angles between surfaces and between the surface and given directions in space.

Surfaces on a crystal are conveniently depicted in a stereographic projection [15, 16]. To briefly describe this, we imagine the crystal in the center of a sphere, and we draw radii perpendicular to each surface from the center of the crystal until the sphere is intercepted (for cubic crystals, these radii will follow the direction of the vector defined by the three Miller indices of each surface). In this way, each surface is projected as a pole on the surface of the sphere. Finally, the poles on the surface of the sphere are projected onto a plane following the strategy illustrated in Figure 1.3. Imagine we put the sphere tangent to a plane at its north pole and we put a light source on the south pole. Then, poles on the sphere will cast shadows on the plane: these are their stereographic projections. The equator of the sphere will define a circle on the plane. Poles on the northern hemisphere of the sphere will cast their shadows inside this circle, while the projection of the poles in the southern hemisphere will lie outside this circle, with their projection being further apart from the circle as the poles are closer to the south pole of the sphere. To avoid this situation, it is customary to interchange the position of the plane and the light to project the poles on the southern hemisphere, so all poles are projected inside the circle defined by the equator of the sphere. Figure 1.3b shows the procedure for the projection from a side view for a pole with $x = 0$. From this view, it can be easily realized that it is equivalent to project the poles on the plane tangent to the sphere, as described earlier, or on the circle defined by the equator of the sphere. The side view allows getting the following relationship between the vector that defines the pole and the x' and y' coordinates of its projection:

$$x' = \frac{x}{1+z}$$

$$y' = \frac{y}{1+z} \tag{1.1}$$

where x' and y' are the coordinates of the point in the projection and x, y, z are the coordinates of the pole on the 3D sphere. A rotation of the three axes might be

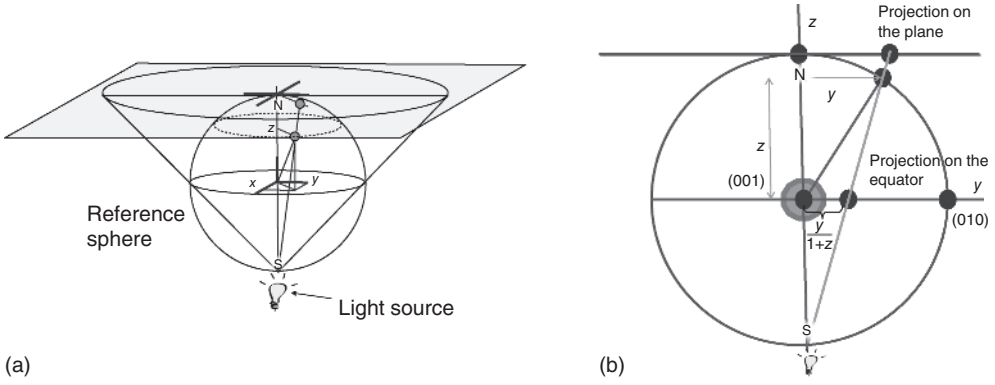

Figure 1.3 Schematic diagrams illustrating the procedure for obtaining the stereographic projection of the faces of a crystal. (a) 3D representation showing the reference sphere and the projection for a general pole with three coordinates *x*, *y*, *z*. (b) Side view and projection of a pole with $x = 0$.

necessary to calculate *x*, *y*, and *z* if the crystallographic axes are not aligned with the Cartesian axis in space.

In what follows, we assume that the crystal belongs to the face-centered cubic system, since this is the system of the most electrocatalytic metals used in electrochemistry (Pt, Rh, Pd, Ag, Ir, etc.). Figure 1.4 shows a stereographic projection of several characteristic surfaces in a cubic crystal. As is evident, the large symmetry in this family of crystals is also translated into the stereographic projection. In fact, the stereographic triangle depicted in Figure 1.4b contains a minimum set of surfaces in such a way that all other surfaces can be obtained from those in the chosen stereographic triangle by symmetry operations. In other words, any surface outside the triangle is equivalent, by symmetry operations, to another surface inside the triangle.

This is reflected in the Miller indices. Any surface of the crystal with Miller indices (*hkl*) can be translated inside the triangle by simple permutation of the three Miller indices and some sign changes. For instance, surface (714) will be equivalent to surface (147) inside the selected stereographic triangle. Surfaces transformed in this way will be either identical or mirror images of each other, depending on the symmetry operations that have been used to bring the surface into the stereographic triangle.

Corners of the stereographic triangle are called *basal planes* and are the simplest surfaces that can be obtained. In this case, the centers of the atoms on the surface define a perfect 2D flat plane, without steps or kinks. Figure 1.5 shows the relationship between the basal planes and the atoms on the unit cell of the crystal. Indicated in the figure are the vectors that characterize the most important directions on the surface. Another important parameter is the area of the unit cell, since it allows calculating the density of atoms on the surface according to

$$N_{hkl} = \frac{n}{S_{hkl}} \tag{1.2}$$

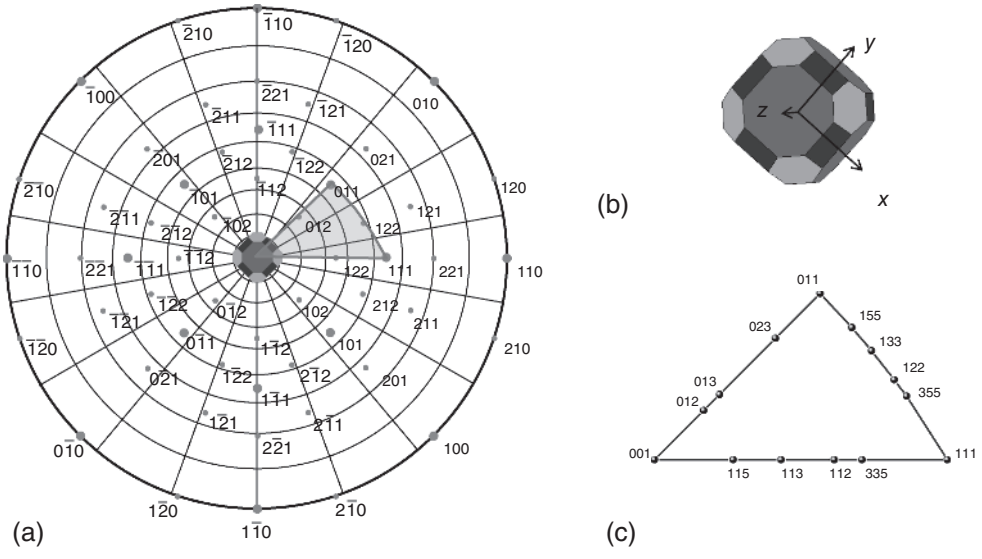

Figure 1.4 (a) Stereographic projection of the main poles for a cubic crystal. The (001) axis has been oriented perpendicular to the plane of the paper. (b) Enlargement of the crystal model, showing the crystallographic axis. The crystal has been slightly tilted to show the (100), (110), and (010) faces, which would be otherwise perpendicular to the paper. (c) Stereographic triangle containing a representative subset of surfaces. All other surfaces can be obtained from those in the triangle by symmetry operations.

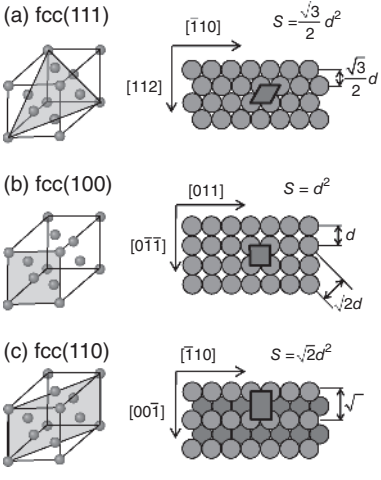

Figure 1.5 Atomic structure of basal planes for an fcc crystal.

where n is the number of atoms in the unit cell and S_{hkl} is its area. For the (111) and (100) planes, $n = 1$. For the (110), n depends on whether we count the atom on the second level or not. Usually, this atom is not available for a surface reaction and also $n = 1$. For the point of view of an electrochemical study, more important than the surface atomic density is the charge corresponding to one electron per

surface atom. This can be easily obtained for each surface as

$$q_{hkl} = \frac{n\,e}{S_{hkl}} \tag{1.3}$$

where e is the elementary charge. The distance between layers, measured perpendicular to the surface, is another important parameter than can be obtained from the hard sphere model of the crystallographic structure of the metal. For face-centered cubic crystals, the following formula provides the interlayer spacing [15]:

$$d_{hkl} = \begin{cases} \frac{a}{\sqrt{h^2+k^2+l^2}} & h,k,l \text{ all odd} \\ \frac{a}{2\sqrt{h^2+k^2+l^2}} & h,k,l \text{ not all odd} \end{cases} \tag{1.4}$$

where $a = \sqrt{2}d$ is the length of the cubic unit cell. Table 1.1 summarizes the previously introduced parameters for the three basal planes and the values of the charge for a monolayer in the case of platinum.

The sides of the stereographic triangle correspond to stepped surfaces composed of terraces and steps with the symmetry of the basal planes at both ends of each side. In this way, surfaces whose stereographic projection lies on the line that joins the (111) and (100) poles are composed of either (111) terraces separated by monoatomic (100) unidimensional steps or (100) terraces separated by (111) monoatomic steps. The geometry of the terrace is given by the pole that is closer, while the other pole determines the symmetry of the step. The Lang, Joyner, and Somorjai (LJS) nomenclature is very useful to designate these stepped surfaces [18]. A surface designed as Pt(S)-[n(111)×(100)] will be composed by (111) terraces with n atomic rows, separated by (100) monoatomic steps. The (S) after the Pt stands for "stepped surface." Table 1.2 summarizes the relations between the LJS notation and the Miller indices for the stepped surfaces in the three crystallographic zones. In each zone, there will be a particular orientation in the middle, containing one row of atoms of one symmetry and one row of atoms of the other. In this case it is arbitrary what is called *terrace* and what is called *step*: this is the turning point of the zone.

Figure 1.6 shows two examples of stepped surfaces. In Figure 1.6A the symmetry of the step has been indicated with a different color. For the surface with

Table 1.1 Area of the unit cell (S), atomic density (N), and charge corresponding to one electron per surface atom (q_{ML}) for the three platinum basal planes.

	$S\times10^{16}$ (cm^2)	$N\times10^{-15}$ (cm^{-2})	q_{ML} (μC cm^{-2})
Pt(111)	6.67	1.50	240.3
Pt(100)	7.70	1.30	208.1
Pt(110)	10.89	0.92	147.2

The atomic diameter has been calculated from the lattice parameter of solid platinum [17] ($a = 0.39236$ nm), according to $a = \sqrt{2}d$.

Table 1.2 Relationship between Miller indices and the Lang, Joyner, and Somorjai nomenclature for stepped surfaces.

Zone	LJS notation	Miller indices	LJS notation	Miller indices
$[1\bar{1}0]$	Pt(S)-$[(n(111)\times(111)]$ Pt(S)-$[(n-1)(111)\times(110)]$	Pt($n\ n\ n-2$)	Pt(S)-$[n(110)\times(111)]$	Pt($2n-1\ 2n-1\ 1$)
$[01\bar{1}]$	Pt(S)-$[n(111)\times(100)]$	Pt($n+1\ n-1\ n-1$)	Pt(S)-$[n(100)\times(111)]$	Pt($2n-1\ 1\ 1$)
[001]	Pt(S)-$[n(100)\times(110)]$	Pt($n\ 1\ 0$)	Pt(S)-$[n(110)\times(100)]$	Pt($n\ n-1\ 0$)

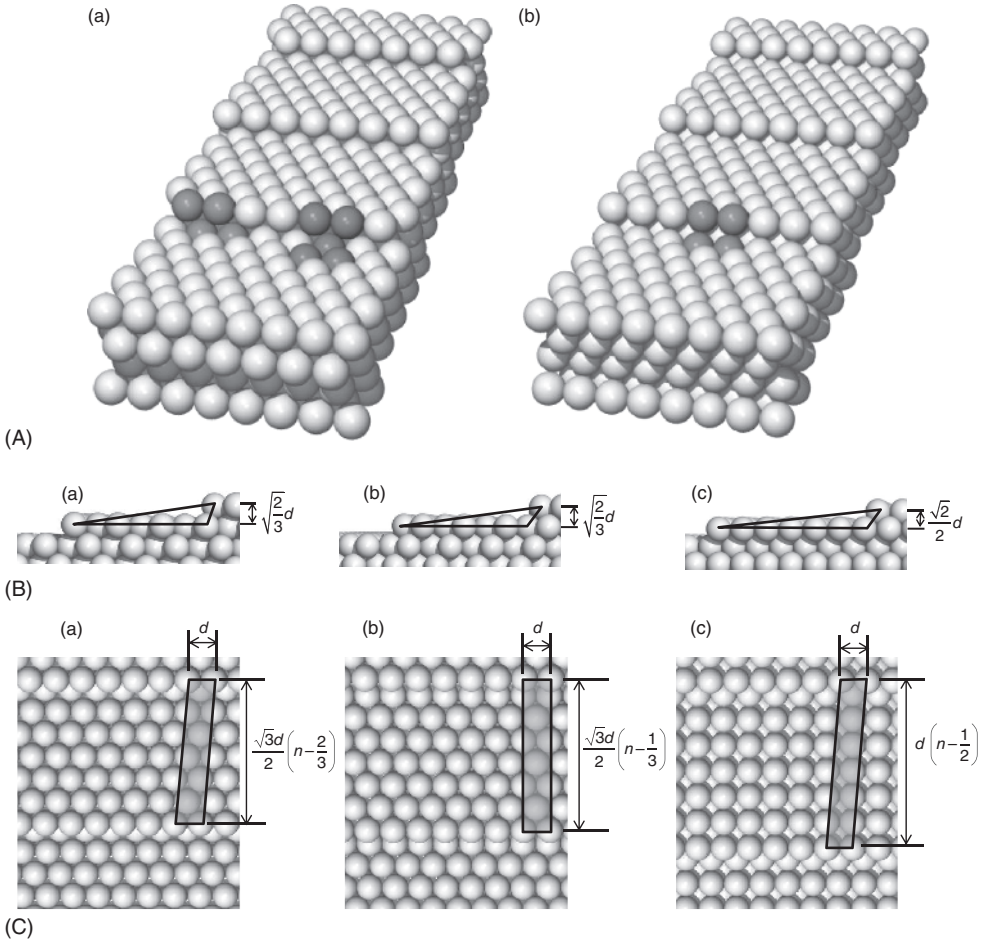

Figure 1.6 Hard sphere model of stepped surfaces for an fcc crystal: (A) tilted view; (B) side view, showing interlaying spacing; and (C) top view, showing dimensions of the unit cell, projected on the plane of the terrace. (a) $(775) = 7(111)\times(111)$; (b) $(433) = 7(111)\times(100)$; and (c) $(13\ 1\ 1) = 7(100)\times(111)$.

(111) terrace and (110) step, the latter can also be understood as a $(11\bar{1})$ step. As before, the dimensions of the unit cells are important to determine the charge corresponding to one monolayer. Such dimensions are indicated in Figure 1.6B,C for some of the step and terrace combinations that more often occur in the literature. Additional information can be obtained elsewhere [19]. In the case of stepped surfaces, the atoms on the surface can be classified according to their environment. Usually, distinction is made between terrace and step atoms. In this way, one can calculate the charge corresponding to one electron per terrace atom or the charge of one electron per step atom. Later we show how these calculated charges compare with the charges measured voltammetrically. One additional parameter important to characterize stepped surfaces is the step density. This is the number of steps per unit of length, measured in the direction perpendicular to the step. This can be easily calculated from the dimensions of the unit cell depicted in Figure 1.6, as the inverse of the length that separate two steps.

Finally, surfaces in the center of the stereographic triangle can also be considered as stepped surfaces with terraces separated with monoatomic steps although now the step is not (infinitely) linear but it is truncated with kinks or corners (zero dimensional). Figure 1.7 exemplifies one of these surfaces. Therefore, surfaces in the center of the stereographic triangle involve sites (or microfacets) with symmetries involving the three basal planes. It has been demonstrated that such surfaces are chiral, that is, they cannot be overlaid with their mirror image and indeed have chiral activity [20–23]. Moreover, while surfaces in the edges of the stereographic triangle are not affected by the permutation of Miller indices (775, 757, and 577 are exactly identical surfaces), permutation of indices of surfaces inside the stereographic triangle will produce equivalent surfaces but with different chirality. A nomenclature has been devised to assign the R or S descriptor to the surface following the Cahn–Ingold–Prelog rule, with the priority being (111) > (100) > (110) [20–22].

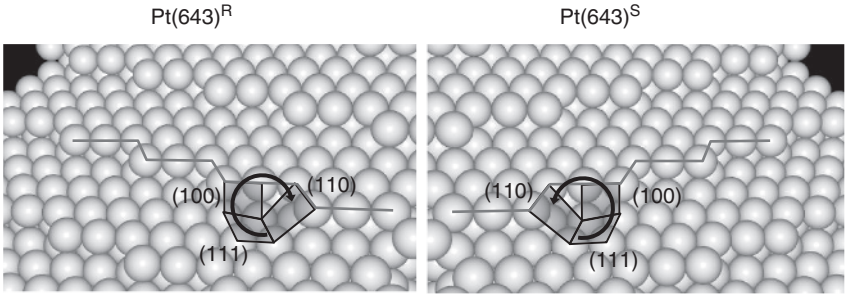

Figure 1.7 Hard sphere model of two kinked surfaces, (643), with same distribution of terrace, steps, and kinks but with different chirality. The Cahn–Ingold–Prelog rule is illustrated in the figure.

1.3
Preparation of Single-Crystal and Well-Oriented Surfaces

The preparation of a well-defined surface starts with the preparation of a single crystal, that is, a macroscopic piece of material in which the atoms occupy positions in the space according to a single set of crystallographic axis. The opposite is a polycrystal, composed of different grains of the material, where adjacent grains do not match a single crystallographic network. The second step will be the identification of the orientation of the crystal by the identification of the direction of the crystallographic axis. Finally, the crystal has to be cut to expose a macroscopic surface that can be used in electrochemical experiments.

In the following, the method used in our laboratory for the preparation of well-defined electrode surfaces will be described [12]. This method has been successfully applied to prepare Pt, Au, Pd, Rh, and Ir surfaces.

The first step is the preparation of the single crystal by carefully melting the end of a high-purity wire of the desired metal. This is done using a sufficiently small H_2 (or butane)/O_2 flame. For reactive metals, inductive heating has also been successfully applied, with the advantage that, in this case, a controlled atmosphere can be used [24]. One key point to obtain a high-quality single crystal is the rate of cooling down the drop of melt metal. This can usually be adjusted by moving the flame up and down or by decreasing the flux of the fuel to the flame. The solidification should be done at a sufficiently slow rate to allow formation of a single crystal. In this process, vibrations should be avoided. The quality of the crystal obtained in this way can be judged by careful observation of the flat facets formed on its surface or by their reflection of light. These facets correspond to the (111) orientation and should define characteristic angles. Normally, observation of the facets with the naked eye or with a magnifying glass allows a preliminary indication of whether a true single crystal has been obtained.

For a better measurement of the angles between the facets, the crystal can be positioned in the center of a goniometer head, and a visible laser beam can be used to identify the direction perpendicular to each facet with high precision. When incident beam and reflected beam are in the same direction, the facet will be perpendicular to the laser. Then, the rotation of the goniometer necessary to bring a second facet perpendicular to the direction of the beam gives the angle between the two facets.

The same optical bench allows the orientation of the crystal before the polishing. The stereographic projections of Figures 1.8 and 1.9 illustrate the process. The starting point is with the crystal positioned with two vertical (111) facets. This means that there will be two laser reflections in the horizontal plane. When one reflection faces the direction of the laser, a second (111) reflection will be on one side, and another (100) reflection will be also in the horizontal plane but on the other side. The polishing disk is perpendicular to the laser beam. Bringing one (111) facet perpendicular to the laser beam allows cutting and

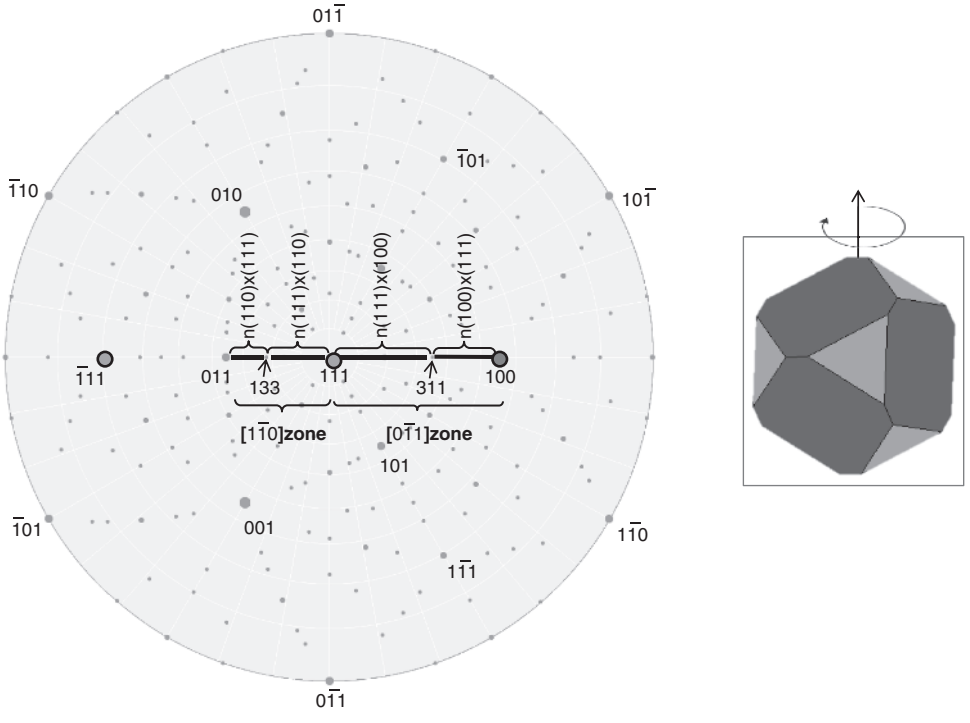

Figure 1.8 Orientation of the crystal and necessary rotations for the preparation of any stepped surface in the zones [1$\bar{1}$0] and [0$\bar{1}$1].

polishing for the preparation of a (111) surface. Rotating the crystal around a vertical axis, an angle equal to 70.53° will bring the second (111) facet perpendicular to the laser beam. Exactly between these two (111) facets, at 35.26°, there will be a (110) surface, whose reflection is not visible, because it does not generate a flat surface. Rotating angles between 0° and 22.00° in the direction of the (110) allows preparation of stepped surfaces with (111) terraces and (110) steps, while angles between 22.00° and 35.26° in the same direction will result in surfaces with (110) terraces and (111) steps. At 22.00° we have the turning point of the zone (331). On the other hand, rotating 54.7° (half of 109.4°, the tetrahedral angle) in the opposite direction will bring the (100) surface to the center. Angles between 0° and 29.50° will produce stepped surfaces with (111) terraces and (100) steps, and angles between 29.50° and 54.7° will produce surfaces with (100) terraces and (111) steps. Again, 29.50° will define the corresponding turning point (311). Given the Miller indices of the desired surface in one of those zones, the angle that has to be rotated from the (111) surface can be obtained by

$$\beta = \cos^{-1}\left(\frac{h+k+l}{\sqrt{3(h^2+k^2+l^2)}}\right) \tag{1.5}$$

To prepare stepped surfaces in the zone between the (100) and (110) or any other surface in the center of the stereographic triangle, two rotations are necessary. A first rotation around the horizontal axis will bring the pole of the desired surface to the horizontal plane. Then, a second rotation around the vertical axis will bring the desired surface to the center of the stereographic projection. The angle of the first rotation can be calculated considering the projection of the (*hkl*) vector on the plane perpendicular to the (111) vector (the (111) plane). This vector can be calculated as the triple product:

$$(rst) = (111) \times ((hkl) \times (111)) \tag{1.6}$$

The angle that we seek is that between the projected vector (*rst*) and the vector $(2\bar{1}\,\bar{1})$. The latter is the projection of the vector (100) on the (111) surface, as can be verified using again Equation 1.6. Therefore

$$\alpha = \cos^{-1}\left(\frac{2r - s - t}{\sqrt{6(r^2 + s^2 + t^2)}}\right) \tag{1.7}$$

The angle of the second rotation is still given by Equation 1.5. The procedure is exemplified in Figure 1.9 for the particular case of the kinked surface with Miller indices (421). In this case, $\alpha = 19.11°$ and $\beta = 28.13°$.

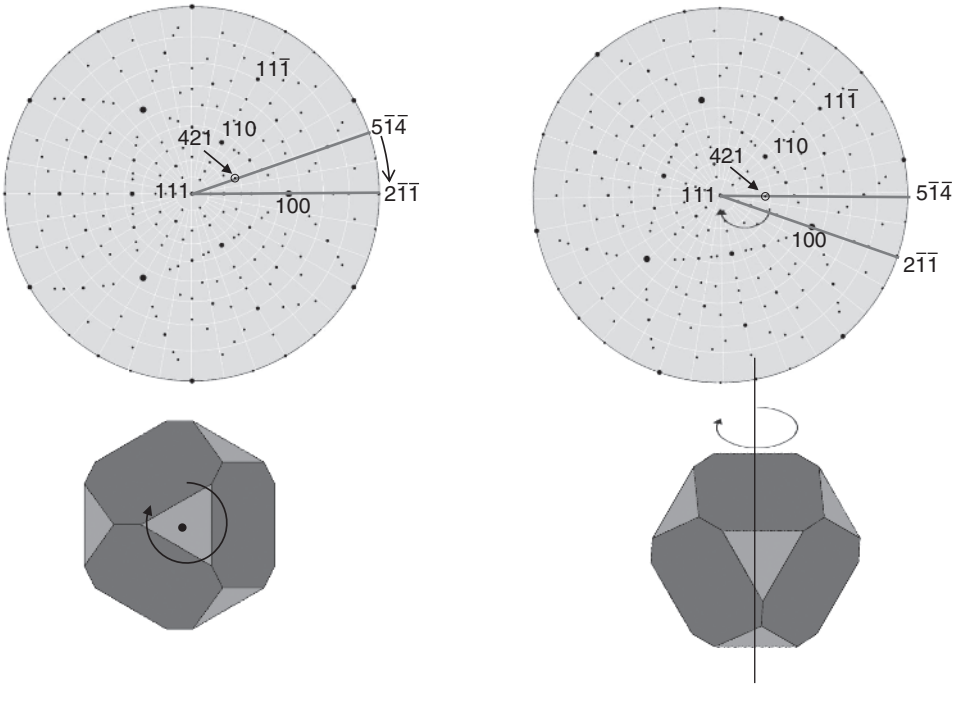

Figure 1.9 Orientation of the crystal and necessary rotations for the preparation of the surface with Miller indices (421).

Before cutting and polishing the crystal, it is immobilized using a suitable epoxy resin. Then, the crystal is first cut using emery paper to expose a circular surface. Normally, the cutting process stops when the maximum diameter has been obtained. Second, the surface is polished using diamond paste or alumina paste until a mirror finish is obtained. The epoxy resin is dissolved using an appropriate solvent such as chloroform. The resulting electrode has the shape of a hemisphere, typically of 2–4 mm diameter, conveniently joined at the end of a wire, which serves to make the electrical contact.

The last particle size using during the polishing is typically 0.25 μm. This is huge in comparison with atomic dimensions. This means that, although the surface appears perfectly flat to the naked eye, that is, mirror polishing quality, at atomic resolution (e.g., Scanning Tunneling microscopy (STM)), it should be very rough. For this reason, the last step after polishing is the annealing of the surface at high temperature, which allows the reordering of the surface according to the selected orientation. The temperature of a butane Bunsen flame is adequate for platinum, since allows enough mobility of the atoms without the danger of melting the crystal. For gold electrodes, annealing of the crystal should be carefully done since the temperature of the Bunsen flame may melt the crystal. Alternatively, the electrode can be annealed at high temperature in an oven for a sufficiently long period (several hours).Finally, the area of the flat surface of the crystal is determined by using a microscope, and the electrode can be conveniently stored.

The last step just before every electrochemical experiment would be the cleaning of the surface. Cleaning of polycrystalline materials is typically done by polishing with alumina followed by electrochemical activation. Such procedure cannot be done with well-defined surfaces since it would lead to the disordering and roughening of the surface. Before the introduction of the flame annealing technique for decontamination of platinum single crystals, early attempts were done to clean the crystal in UHV with strict control of the surface quality and then to transfer the electrode to the electrochemical cell [4–8]. However this proved to be really difficult, resulting almost always in a partially contaminated surface and, more importantly, irreproducible results from different laboratories.

In 1980, the French scientist Jean Clavilier published for the first time the decontamination of a platinum single crystal just by heating it a few seconds in a hydrogen flame [2, 3]. Thanks to the high catalytic ability of platinum, the high temperature promoted the oxidation of any organic contamination that might have been present on the surface. In addition, the high temperature also increased the mobility of atoms, facilitating the reordering of the surface. While the electrode was still hot, it was rinsed with high-purity water, which cooled down the electrode and led to the formation of a drop of water that protected the surface from being contaminated with gases present in the atmosphere of the laboratory [25]. The protected electrode was then transferred to the electrochemical cell and contacted with the solution, adopting the hanging meniscus configuration [25, 26].

After the publication of the first voltammogram of platinum single crystal obtained by this method, some controversy arouse since a significantly different

voltammogram was obtained in comparison with all the other attempts performed by other labs until this moment [11]. It was later demonstrated that the voltammogram obtained for a flame annealed (111) electrode is the correct one corresponding to the clean and ordered surface [10, 11, 27]. However, for (100) and (110) and any other stepped or kinked surface, it was later demonstrated that cooling of the crystal after flame annealing should be done in a reducing atmosphere, in the absence of O_2 [28–30]. As will be discussed in the following, oxidation of the surface causes its disordering. For that reason, cooling is done in a H_2 + Ar atmosphere that avoids oxidation after flame annealing.

1.4
Understanding the Voltammetry of Platinum

Figure 1.10 shows the voltammetry obtained with the three basal planes of platinum in two different electrolytes: 0.1 M $HClO_4$ and 0.5 M H_2SO_4. Perchloric acid is selected since it is usually accepted that perchlorate anions do not adsorb specifically on the surface. Conversely, (bi)sulfate anions are usually strongly adsorbed, thus shifting the voltammetric features to low potentials. The limits of the potential sweep are imposed by the onset of hydrogen evolution below 0.06 V and the onset of oxide formation around 0.9–1.0 V. Use of a reversible hydrogen electrode (RHE) is convenient here since both potential limits shift with pH in the same way as the RHE. Oxide formation should be avoided since the subsequent reduction causes surface disordering [10, 27, 31].

The first observation after looking at Figure 1.10 is that strong differences are obtained between the three basal planes, suggesting that the electrochemical

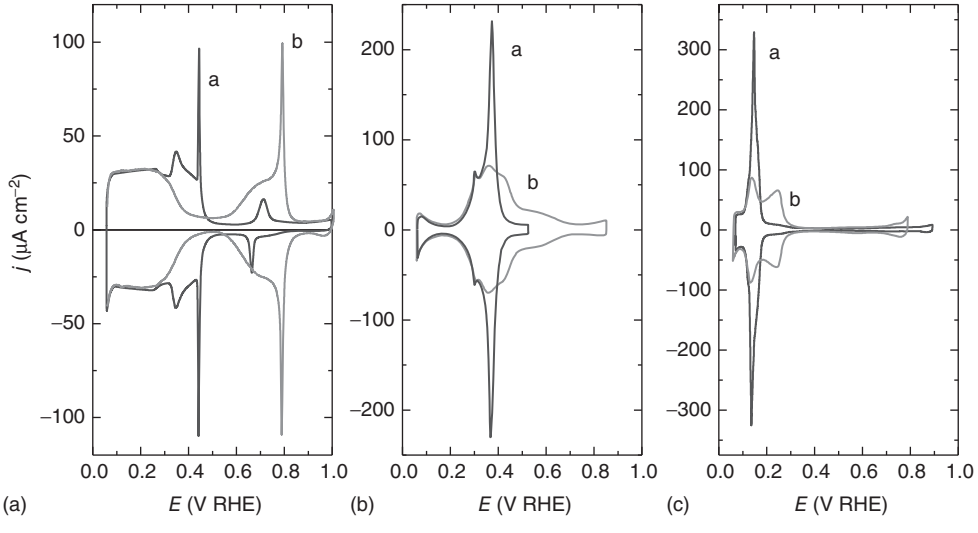

Figure 1.10 Cyclic voltammograms for the three Pt basal planes in (a) 0.5 M H_2SO_4 and (b) 0.1 M $HClO_4$. (A) Pt(111); (B) Pt(100), and (C) Pt(110). Scan rate: 50 mV s^{-1}.

phenomena responsible for the observed voltammetric features are strongly sensitive to the arrangement of atoms on the surface of the electrode.

The voltammograms consist of a series of peaks located at different potentials and with different width and shape. The peaks observed in the positive- and negative-going potential sweeps are mirror images of each other, indicating that the process is reversible. Moreover, variation of the scan rate reveals a linear dependence of the current with this parameter, suggesting that all these peaks correspond to adsorption processes.

The voltammetric response to reversible adsorption processes is given by the adsorption isotherm, that is, the functional relationship between the adsorption coverage, θ, and electrode potential. For an electrosorption process involving the oxidation or reduction of the adsorbing species, charge and coverage are intimately related [32]:

$$q = zF\Gamma_{max}\theta \tag{1.8}$$

Therefore, the voltammetric current is determined by the adsorption isotherm:

$$j = zF\Gamma_{max}\frac{d\theta}{dt} = zF\Gamma_{max}\frac{d\theta}{dE}\frac{dE}{dt} = zF\Gamma_{max}\frac{d\theta}{dE}\nu \tag{1.9}$$

This equation demonstrates the linearity between current and scan rate. It can be easily demonstrated that for an adsorption process that follows a Frumkin isotherm [32]:

$$\frac{\theta}{1-\theta} = \exp\frac{\Delta G^0}{RT}\exp\frac{zFE - r\theta}{RT} \tag{1.10}$$

The voltammetric feature associated with this process is a symmetric peak, in which the peak potential gives a measure of the adsorption energy, the width of the peak is related with the lateral interaction parameter, r, and the area under the peak is related with the coverage. For an irreversible process, the coverage will depend on time, not only on potential, and Equations 1.9 and 1.10 do not hold.

In consideration with the voltammetry of platinum single crystals, the appearance of different peaks points out the existence of different processes. Different peaks do not necessarily mean different adsorption species, but can be the same species on different adsorption sites of the surface. This would result in different adsorption energies and different lateral interactions and therefore a different voltammetric response.

Let us start with the profile of Pt(111) in 0.5 M H_2SO_4, the best interface for electrochemical characterization under ultrapure conditions. A small minimum in the current at about 0.32 V separates two regions in the voltammogram. A relatively flat current is observed between 0.06 and 0.3 V. At higher potentials, a peak at 0.35 V is followed by a sharp spike at 0.44 V. After this spike, the current drops to nearly capacitive values, except for a small couple of quasireversible (asymmetric) peaks around 0.71/0.66 V. One clue to understand the voltammetric profiles of Figure 1.10 is the comparison between the charge density and the atomic density for each electrode. Leaving aside the small pair of peaks at higher potentials, the

charge integrated between 0.06 and 0.6 V is nearly 240 μC cm^{-2}, after subtracting the double-layer contribution. This number coincides rather precisely with the charge corresponding to the interchange of one electron for each platinum atom on the (111) surface (Table 1.1). This coincidence led, in the early interpretation of this voltammogram, to the conclusion that current in this potential range corresponds to the adsorption of a single species, namely, hydrogen, reaching a coverage of 1 before starting H_2 evolution [3, 9, 11]. However, this conclusion was not followed by all the electrochemists for the following reasons: (i) Hydrogen adsorption had never been observed on platinum at such high potentials. (ii) If 0.1 M $HClO_4$ was used instead of 0.5 M H_2SO_4, the two regions mentioned earlier separate, with the low potential region remaining essentially unaltered and the high potential region shifting to even higher potential values. (iii) Mixtures of perchloric and sulfuric acid showed that the high potential region exhibits a Nernstian dependence with the sulfate concentration [33]. Therefore, a second interpretation was that the low potential region corresponds to hydrogen adsorption, while the high potential region is anion adsorption, according to the equations [10, 33]

$$\begin{aligned} &Pt - H + H_2O \rightarrow Pt + H_3O^+ + e \\ &Pt + A^- \rightarrow Pt - A_{ads} + e \end{aligned} \tag{1.11}$$

The problem to distinguish both processes is that both produce oxidation currents during the positive scan of the potential. However, during the positive scan, hydrogen would be decreasing its coverage, while the anion coverage would be increasing.

1.4.1 CO Charge Displacement Experiment

The idea behind the displacement experiment is that by imposing the direction of the reaction, that is, in the direction of desorption, it is possible to distinguish the reductive desorption of an anion from the oxidative desorption of a cation (hydrogen). To achieve the desorption at constant potential, a displacing agent is introduced into the system. This agent should be a species that adsorbs stronger than the adsorbates that have to be displaced, in this case, the hydrogen and the anion. By recording the current during the displacement process, not only the nature of the adsorption (cationic or anionic) can be discerned from the sign of the current, but also the amount of adsorbed species can be quantified from the displaced charge.

A good displacing agent should comply with the following characteristics: (i) Should be strongly adsorbed on the surface of the substrate. (ii) Its adsorption should be neutral and, therefore, should not contribute to the charge being displaced. (iii) Should be easily introduced into the cell without other interferences. Regarding the last point, oxygen should be avoided during the introduction of the displacing agent to avoid negative currents due to oxygen reduction. If a solution is introduced, then it should be properly deoxygenated.

The best displacing agent for probing platinum interfaces turned out to be CO [34–40]. This adsorbs very strongly on platinum without involving charge. Being a gas, it is easily introduced into the cell avoiding the interference of oxygen. In addition, CO has two other advantages. The excess of CO can be easily removed from the solution just by Ar bubbling, and then, CO can be oxidatively stripped from the surface at reasonably low potentials, allowing testing the final state to make sure that surface order and cleanliness has been preserved during the whole process.

The CO displacement is performed as follows [39]: (i) The initial voltammogram is recorded to make sure that the surface is clean and well ordered. (ii) The electrode potential is fixed at the desired value. (iii) CO is introduced into the system allowing the diffusion through the solution toward the interphase. During CO adsorption, current flows as a consequence of the displacement of the interphase. (iv) When displacing current drops to zero, CO flux is stopped, and Ar is bubbled during a suitable time to remove all the CO from the solution. (v) CO remains adsorbed on the surface, as can be checked by recording the voltammogram again after Ar bubbling in the low potential range. (vi) Finally, the high potential limit is increased to allow the oxidation of adsorbed CO, resulting in a clean surface. By returning the potential to the initial value fixed in (ii), the cycle is closed and the final state of the surface should be identical with the initial state.

The validity of the CO displacement method, particularly the assumption that CO adsorption does not involve charge transfer, was tested by displacing an iodine adlayer [35]. The structure and coverage of this adlayer was well known from a variety of methods, including *in situ* STM and *ex situ* Auger Electron Spectroscopy (AES) and Low energy electron diffraction (LEED) [35]. Good consistency between experimental displaced charges with those predicted from the coverage of the adlayer supports the validity of the method [35].

Another displacing agent that has been successfully used is I_2 [41]. This adsorbs in a potential region nonaccessible by CO due to the oxidation of the latter. However, when I_2 is introduced into the solution, it cannot be easily removed, and therefore, the whole solution should be exchanged before a new experiment can be performed. The results of iodine displacement are consistent with the interpretation of the CO displacement [41].

For Pt(111) in 0.5 M H_2SO_4, the charge displaced at 0.08 V amounts to about 150 $\mu C\,cm^{-2}$, while the charge displaced at 0.5 V is about $-90\,\mu C\,cm^{-2}$ [37]. The negative sign of the charge displaced at high potentials demonstrates that adsorption states above 0.30 V are due to anion adsorption. Therefore, the coincidence between the integrated charge in the whole potential region and the charge corresponding to a monolayer is just casual. Now we can understand the voltammetry depicted in Figure 1.10A for Pt(111). Starting at the lower limit of potentials, the surface is covered with nearly two-thirds of a monolayer of hydrogen. As the potential is increased, the hydrogen coverage decreases and a positive current flows. At around 0.3 V, almost all of the hydrogen has been desorbed and sulfate starts to be adsorbed on the free sites of the surface. This pushes out the small amount of hydrogen remaining above 0.3 V. Sulfate

adsorption initially forms a disordered adlayer. At about 0.44 V, sulfate coverage is high enough so the attractive lateral interactions force the formation of an ordered adlayer, causing a sudden change in the double-layer capacity, resulting in the sharp spike at this potential. This spike therefore corresponds to a phase transition between a disordered phase of adsorbed sulfate at potentials lower than the spike and an ordered phase of a sulfate adlayer at potentials higher than the spike. The ordered phase has been identified by STM as a $(\sqrt{3} \times \sqrt{7})$ with three of the oxygens in the sulfate molecule coordinated to three platinum atoms on the surface [42, 43]. The sulfate adlayer on Pt(111) has been extensively studied with other complementary techniques such as FTIRRAS [44–54], radiotracers [55], second harmonic generation [56], and STM [42, 43].

In 0.1 M $HClO_4$ the voltammetry of Pt(111) shows two well-separated adsorption regions. The region below 0.40 V corresponds to hydrogen adsorption and desorption. This region is nearly unaffected by the nature of the anion in the electrolyte, and the same charge is displaced at 0.08 V in perchloric and sulfuric acids, corresponding to two-thirds of the monolayer [34]. However, anion adsorption in perchloric acid is displaced to higher potentials, starting at 0.55 V. It is usually assumed that perchlorate anion is a very weak ligand and does not adsorb specifically on metal surfaces. This idea is reinforced by the observation of virtually identical voltammetric profile in fluoride [10, 47, 53] or trifluoromethanesulfonate [57] containing electrolytes, another nonadsorbing anions. If the same voltammogram is observed with several different anions, the adsorbing species must be something else, common to the different electrolytes. Obviously, the common species is the water, and therefore, it is generally accepted that the adsorption states at potentials higher than 0.55 V in perchloric acid (or NaF/HF mixtures or trifluoromethanesulfonic acid) correspond to the formation of adsorbed OH.

For Pt(100) in 0.5 M H_2SO_4, the voltammetric profile is characterized by the observation of a main rather sharp peak at 0.38 V with a smaller peak around 0.31 V. The ratio between the heights of both peaks is very dependent on the quality of the crystal, with the peak at 0.31 being smaller for high-quality crystals. This is also very sensitive to the thermal treatment and the cooling conditions [28, 30, 58, 59]. More information about this peak will be obtained from the analysis of stepped surfaces [60] (see the following text). As before, key information to understand the voltammogram is obtained from the CO displacement experiment. In this case, nearly 200 $\mu C\,cm^{-2}$ is displaced at 0.1 V [38]. This charge fits rather well with that corresponding to a monolayer on Pt(100) (209 $\mu C\,cm^{-2}$), indicating that hydrogen coverage at the lower limit of potentials is near unity. On the other hand, the charge displaced at potentials higher than the peak is negative, signaling that anion adsorption takes place in the high potential range. Therefore, we could conclude that, in this case, both peaks correspond to the replacement of hydrogen by sulfate as the potential is increased. As a difference with Pt(111), in this case hydrogen desorption and anion adsorption are coupled, and sulfate immediately occupies the free sites left by the hydrogen. Comparison of the profiles in perchloric and sulfuric acid shows that hydrogen desorption extends to higher potentials

in the first electrolyte. In fact, in perchloric acid, hydrogen desorption and OH adsorption are more separated. The current between 0.5 and 0.75 V is generally attributed to OH adsorption [61]. As the potential is increased from 0.1 V, hydrogen desorbs initially triggered by the increasing electrode potential, but then, it is pushed out by the adsorbing anion. Since sulfate adsorption starts at lower potentials, the adsorption states are compressed in a narrower potential window. On the other hand, because OH adsorption starts at higher potential, hydrogen remains on the surface until higher potentials in perchloric acid. This picture essentially acknowledges full H monolayer before H_2 evolution. A refined analysis however reveals a more complex situation when stepped surfaces are used. In this respect the minimum observed in the voltammetric curve at 0.2 V defines the adsorption states of the terraces, and adsorption at lower potentials is associated with step/defects [60]. It appears that the more open Pt(100) surface always contains a significant amount of defects (15%) after flame annealing. This could be a consequence of the formation of a reconstructed surface at high temperatures during the annealing [62]. The reconstructed surface is characterized by a higher atomic density, and the subsequent lifting of the reconstruction after contacting the electrolyte would result in the formation of islands to accommodate the extra surface atoms. The STM study of this surface supports this result [58, 59, 63, 64]. The charge trends for stepped surfaces, combining voltammetry and CO displacement data with hard sphere model predictions, suggest that only 85% of the surface atoms are located in 2D flat terraces [60].

A similar explanation can be given for the Pt(110) surface. While the voltammetric charge is about 220 $\mu C\,cm^{-2}$, the displaced charge at 0.1 V amounts to nearly 150 $\mu C\,cm^{-2}$ in both sulfuric and perchloric acids [34, 38]. This charge fits well with the value corresponding to a complete monolayer on Pt(110) (Table 1.1). As the potential is increased in sulfuric acid, a single peak at 0.14 V corresponds to the replacement of hydrogen by sulfate anions. Conversely in perchloric acid, two peaks are observed at 0.14 and 0.25. While it is tempting to assign the first peak to hydrogen desorption and the second to OH adsorption, the charge of the first peak is clearly lower than the 150 $\mu C\,cm^{-2}$, indicating that at least a fraction of the second peak should still correspond to hydrogen desorption. Again, the use of stepped surfaces suggests that a significant fraction (50%) of the surface is not two dimensionally ordered as terraces [65]. Moreover recent results after cooling in CO atmosphere have revealed new voltammetric profiles [66]. These results should be carefully analyzed to reach a better picture of the platinum surfaces, including new experiments and theoretical calculations.

1.4.2
Stepped Surfaces

The use of stepped surfaces allows the systematic modification of the distribution of sites on the surface of the electrode. This approach offers new clues in the understanding of the role of the geometry of each adsorption site on its catalytic activity.

Figure 1.11 shows the cyclic voltammograms of some surfaces in the crystallographic zone between (111) and (110) basal planes. Therefore, these surfaces are composed of (111) terraces of variable length separated by monoatomic steps. In this figure, n represent the number of atomic rows on the terrace. Therefore, as n decreases, the density of steps increases. As the amount of steps increases, a new peak appears in the voltammogram around 0.12 V. Clearly, this peak must be related with the response of the step toward hydrogen and/or anion adsorption. On the other hand, the current between 0.06 and 0.3 V, previously attributed to hydrogen adsorption on the (111) surface, decreases as the length of the terrace decreases. Comparison of the voltammograms obtained for the same stepped surface in 0.1 M $HClO_4$ (Figure 1.11a) and 0.5 M H_2SO_4 (Figure 1.11b) shows that for surfaces with long terraces, the low potential region, below 0.3 V, is virtually unaffected by the nature of the anion in the electrolyte [40]. This would suggest that the new peak associated with the introduction of steps does not contain any contribution from anion adsorption. Alternatively, it could happen that the amount of anion adsorption is given by the site geometry and is independent of the nature of the anion. At higher potentials, anion adsorption takes place on the terrace, either sulfate or OH in the perchloric acid solution. The particular features of the voltammogram just described earlier make it easy to separate the contribution from terrace and steps by integrating the voltammogram taking reasonably unambiguous baselines. These charges can be compared with the hard sphere model introduced in Section 1.2. For this particular family of stepped surfaces, it is necessary to wisely decide what atoms are counted as belonging to the terrace or to the step in the hard sphere model. The reason for this ambiguity lies in the fact that the surface can be described either as containing n atomic rows on the terrace separated by (111) steps or as $(n-1)$ atomic rows on the terrace separated by (110) steps. Figure 1.12a shows how to count the number of atoms on both possibilities, while Figure 1.12b illustrates how the unit cell can be decomposed as a combination of smaller unit cells with the geometry of the basal planes that compose the stepped surface. According to this decomposition, the charge corresponding to one electron per atom on the terrace would be

$$q_{\text{terr}} = \frac{(n-1)e}{S} \quad \text{if the step is considered (111)} \tag{1.12}$$

$$q_{\text{terr}} = \frac{(n-2)e}{S} \quad \text{if the step is considered (110)} \tag{1.13}$$

The charge corresponding to one electron per atom on the step is

$$q_{\text{step}} = \frac{e}{S} \tag{1.14}$$

With S being the area of the unit cell, according to Section 1.2

$$S = \frac{\sqrt{3}}{2} d^2 \left(n - \frac{2}{3}\right) \frac{1}{\cos \beta} \tag{1.15}$$

where beta is given by eq. (1.5)

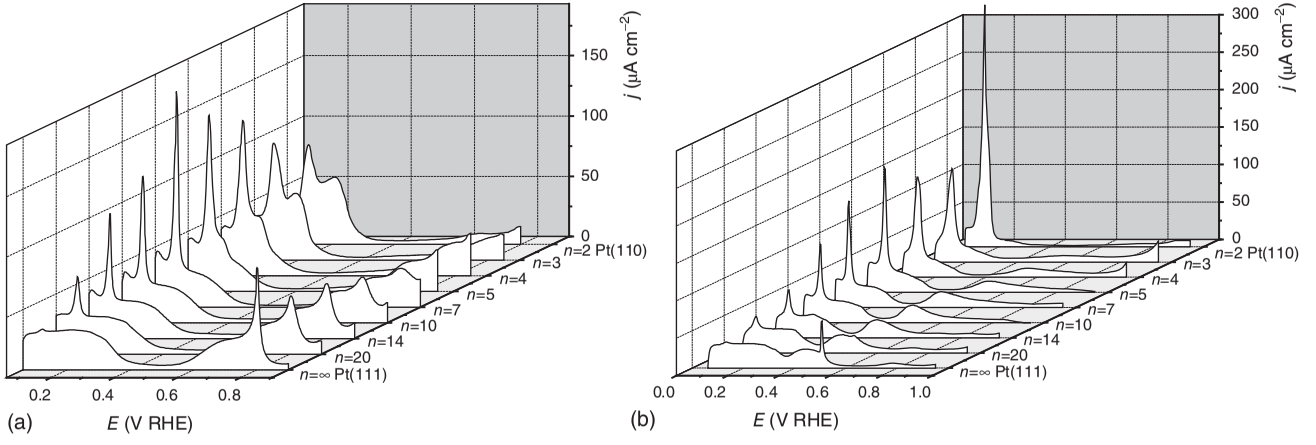

Figure 1.11 Cyclic voltammograms for Pt stepped surfaces in the $[1\bar{1}0]$ zone, Pt(S)-[$(n-1)(111)\times(110)$], with Miller indices Pt($n\ n\ n-2$). (a) 0.1 M $HClO_4$ and (b) 0.1 M H_2SO_4. Scan rate: 50 mV s^{-1}.

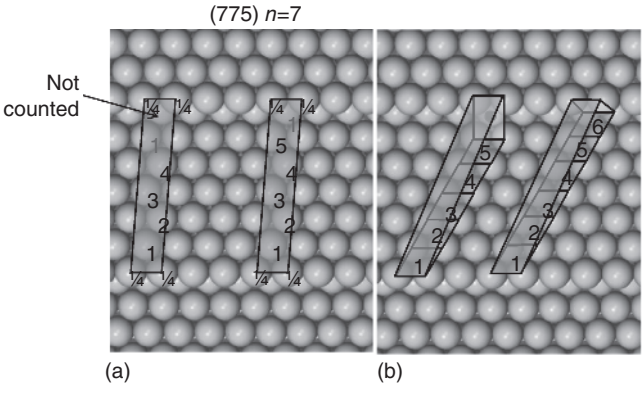

Figure 1.12 Counting the atoms on the (775) surface. (a) Atoms whose center lies inside the unit cell should be counted. The atoms in corner of the unit cell should be counted as 1/4 each one. The atom marked with a light gray "1" is the step atom. (b) Decomposition of the unit cell into terrace and step contributions.

Combination of Equations 1.11 – 1.15 gives

$$\frac{q_{\text{step}}}{\cos\beta} = \frac{2e}{\sqrt{3}d^2}\left(n-\frac{2}{3}\right)^{-1} = q_{111}\left(n-\frac{2}{3}\right)^{-1} \tag{1.16}$$

where the term $\cos\beta$ allows the projection of the experimental area measured in the plane of the $\{hkl\}$ surface to the plane of the {111} terrace. On the other hand, for the charge contribution of the terrace,

$$\frac{q_{\text{terr}}}{\cos\beta} = \theta_{\max} q_{111}\left(1-\frac{1/3}{n-2/3}\right) \quad \text{if the step is (111)} \tag{1.17}$$

$$\frac{q_{\text{terr}}}{\cos\beta} = \theta_{\max} q_{111}\left(1-\frac{4/3}{n-2/3}\right) \quad \text{if the step is (111)} \tag{1.18}$$

The term $\theta_{\max}$ has been introduced to account for the fact that maximum coverage on the (111) terrace is lower than unity. Therefore, plots of projected charges, $\frac{q_{\text{terr}}}{\cos\beta}$ and $\frac{q_{\text{step}}}{\cos\beta}$, as a function of $\left(n-\frac{2}{3}\right)^{-1}$ should give straight lines. From their slopes, some information can be obtained about the real nature of the step, either (111) or (110).

Figure 1.13 shows the comparison between the voltammetric charges and those predicted by the hard sphere model, as indicated earlier. In this figure, the charge density is not referred to the projected area, and, therefore, the lines for the hard sphere model are not perfectly linear. For the charge under the peak at 0.12 V, good agreement is observed with the hard sphere model, at least for surfaces with low step density. This agreement supports the hypothesis that this peak corresponds to hydrogen adsorption on step sites, with negligible contribution from anion adsorption. For the charge of the terrace, good agreement is observed between experimental data and the hard sphere model that considers the step as (110).

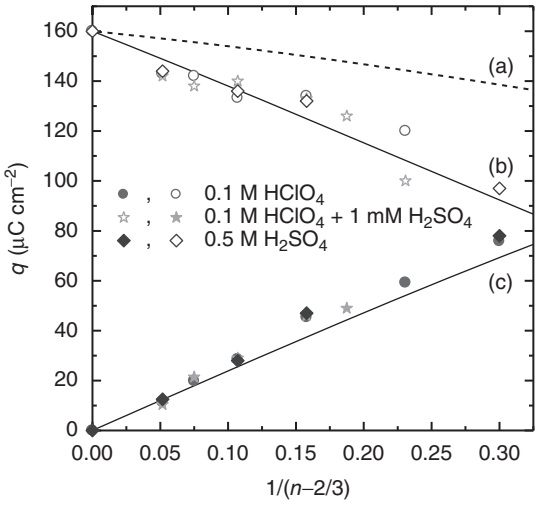

Figure 1.13 Comparison of voltammetric charges (symbols) and charges from the hard sphere model (lines) for Pt(S)[*n*(111) × (111)] stepped surfaces. (i) Terrace charge considering (111) step. (ii) Terrace charge considering (110) step. (iii) Step charge.

This is equivalent to saying that the atom that is below the step is not accessible for hydrogen adsorption.

Deviation between experimental and hard sphere model data is evident for very short terraces, indicating that around the turning points of the zone, the surfaces can hardly be considered as a combination of terrace and steps but should be considered as a new surface by itself. The reason for that is that for short terraces, the electronic perturbation introduced by the step affects the whole terrace, interacting with the next step, a situation that is negligible with larger terraces.

Let us move now to the stepped surfaces with (111) terrace and (100) step. Figure 1.14a shows the voltammograms in perchloric acid, while Figure 1.14b shows them in sulfuric acid. Similarly to what has been described earlier for the stepped surfaces with (110) step, the introduction of steps in this zone also results in a new voltammetric peak, but now shifted to 0.28 V. The relevant equations are now

$$\frac{q_{\text{step}}}{\cos\beta} = \frac{2e}{\sqrt{3}d^2}\left(n-\frac{1}{3}\right)^{-1} = q_{111}\left(n-\frac{1}{3}\right)^{-1} \tag{1.19}$$

$$\frac{q_{\text{terr}}}{\cos\beta} = q_{111}\left(1-\frac{2/3}{n-\frac{1}{3}}\right) \tag{1.20}$$

In this case, stronger deviations are observed when comparing the experimental and theoretical charges, calculated from the aforementioned equations [19]. In addition, comparison of the voltammograms in perchloric and sulfuric acid clearly indicates a role of the anion in the adsorption states associated with the step, with the peak much sharper when sulfate is present.

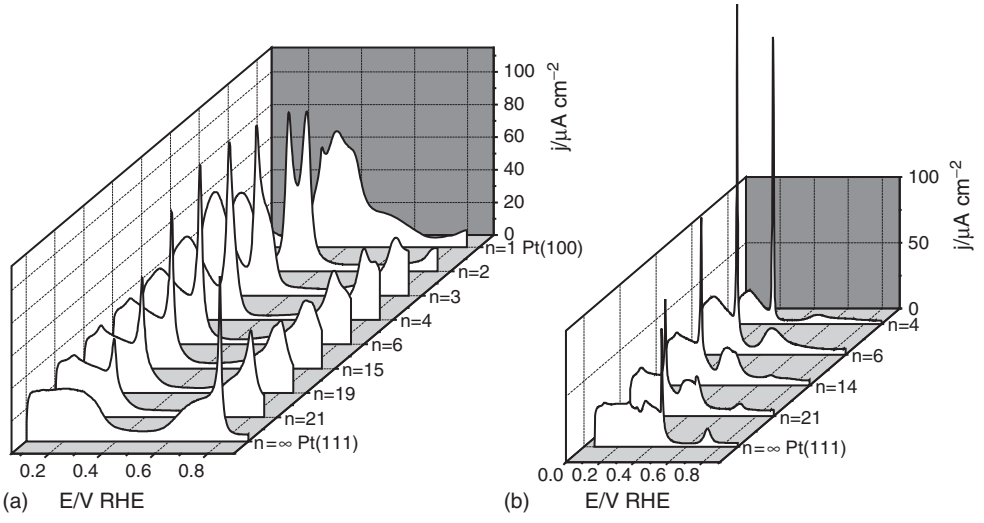

Figure 1.14 Cyclic voltammograms for stepped surfaces in the [01$\bar{1}$] zone, Pt(S)-[n(111) × (100)], with Miller indices Pt(n + 1 n − 1 n − 1). (a) 0.1 M $HClO_4$ and (b) 0.5 M H_2SO_4. Scan rate: 50 mV s^{-1}.

Figure 1.15 shows the voltammograms of some surfaces in the same crystallographic zone but now beyond the turning point, (311). Therefore, these surfaces are composed of (100) terraces and (111) steps. The (311) surface can be described either as a 2(111) × (100) surface or as a 2(100) × (111) surface.

In this respect, the voltammogram of the (100) surface in 0.1 M H_2SO_4 is characterized by a main peak at 0.39 V and a smaller peak at 0.31 V. As new (111) steps are introduced onto the (100) surface, the peak at 0.31 grows (shifting toward 0.28 V) while voltammetric contributions above 0.33 V decrease. In addition, new voltammetric currents develop at potentials below 0.2 V. In consequence, the peak at high potentials should be ascribed with the response of the terrace, while responses at 0.28 – 0.31 V and below 0.2 V correspond to new sites created after the introduction of the steps. More information about the nature of these peaks can be obtained by looking at how the voltammogram changes when we move in the crystallographic zone from n(111) × (100) to n(100) × (111) across the (311) surface. For surfaces with (100) steps and (111) terraces, the contribution of the step appears at the same potential as with surfaces with (100) terrace and (111) step. Therefore, most likely the peak in both situations should correspond to adsorption on sites of similar symmetry. We can therefore state that this peak corresponds to monodimensional (100) sites, either because they are surrounded by two (111) terraces or because they are in the first row of (100) sites on the terrace adjacent to the (111) step. Figure 1.16 illustrates these concepts.

Finally, the contributions below 0.2 V in the voltammograms for the Pt(S)-[n(100) × (111)] stepped surfaces coincide with the potential region of hydrogen adsorption on (111) terraces. Therefore, we can assign this voltammetric region in this family of stepped surfaces to hydrogen adsorption on the (111) steps. The

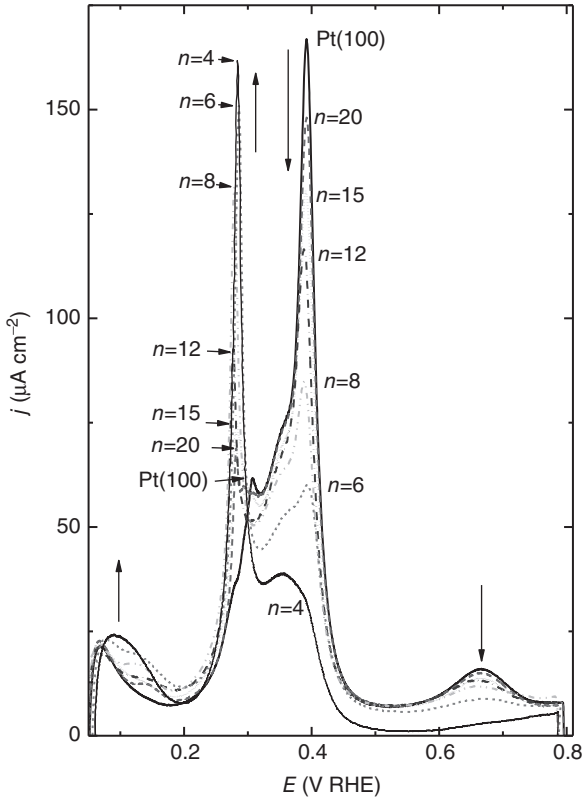

Figure 1.15 Cyclic voltammograms in 0.1 M H_2SO_4 for stepped surfaces in the [01$\bar{1}$] zone, Pt(S)-[n(100) × (111)], with Miller indices Pt($2n-1$ 1 1). Scan rate: 50 mV s^{-1}. Arrows indicate the increase of the step density.

fact that the (100) surface contains nonnegligible charge in this region suggests the existence of a significant density of defects, most likely formed during the lifting of the reconstruction that takes place during flame annealing.

1.5 Potential of Zero Charge of Platinum Single Crystals

The potential of zero charge (pzc) is a fundamental parameter in electrochemistry. Its knowledge, together with that of the differential capacity, allows establishing an unambiguous relationship between the electrode charge and the potential. The concept of pzc was clearly established for liquid electrodes based on electrocapillary measurements. For a metal in contact with a solution of a strong acid HA that dissociates into H^+ and A^-, the electrocapillary equation can be written as [67, 68]

$$-d\gamma = \sigma dE + \Gamma_{H^+} d\mu_{H^+} + \Gamma_{A^-} d\mu_{A^-} \tag{1.21}$$

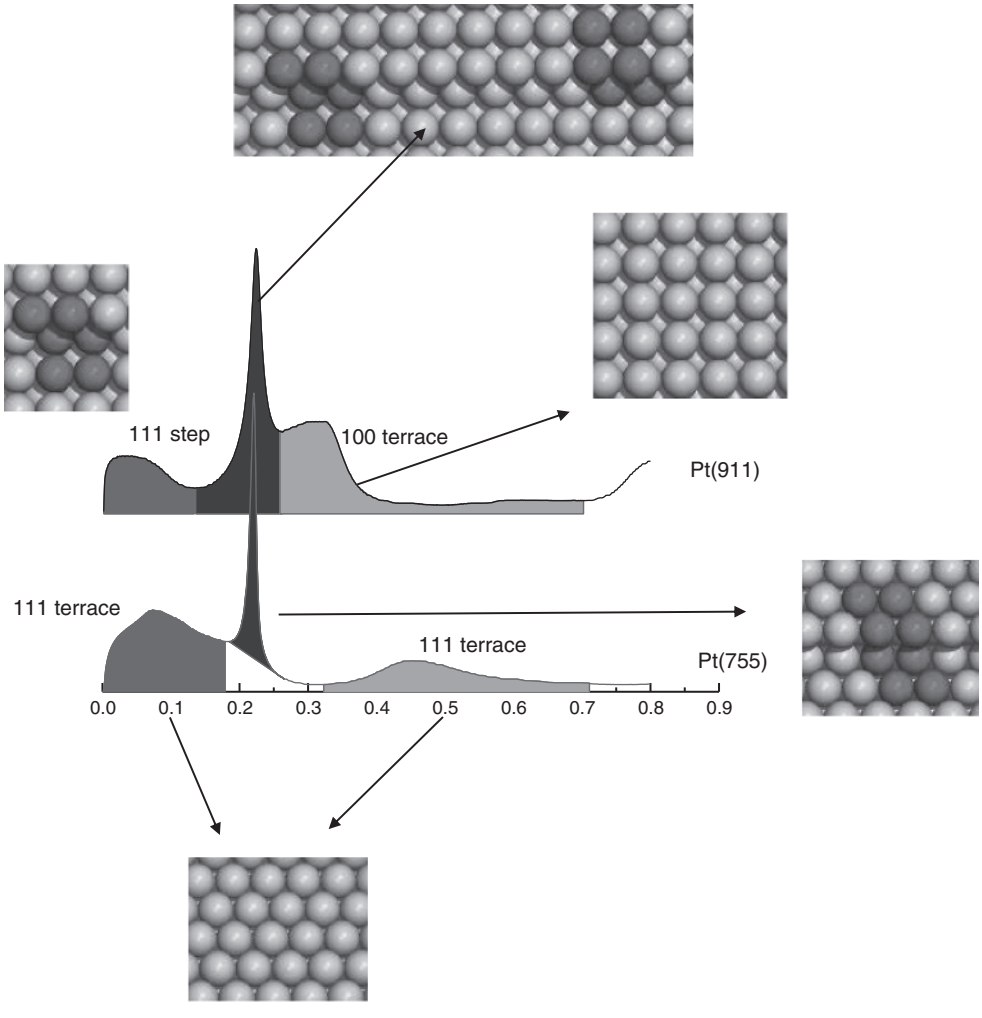

Figure 1.16 Description of different voltammetric peaks to different ensemble of atoms for (100) × (111) stepped surfaces.

In this case, the electrode potential is measured versus a reference electrode insensitive to the concentration of H^+ and A^-:

$$E = \Delta_{\mathrm{M}}^{\mathrm{S}}\Phi - \Delta_{\mathrm{M}}^{\mathrm{S}}\Phi^{\mathrm{ref}} \tag{1.22}$$

The location of the maximum of the electrocapillary curve provided an easy way for the determination of the pzc, according to Lippmann equation [69]:

$$\sigma = -\left(\frac{\partial\gamma}{\partial E}\right)_{\mu_i} \tag{1.23}$$

Several methods were developed for the determination of the pzc of solid electrodes [70]. The most important among them, because it is also applicable

for well-defined surfaces, is based on the identification of the minimum in the differential capacity that, according to Gouy–Chapman theory, should be observed centered at the pzc for diluted solutions in the absence of specific adsorption, if water dipole contributions are considered negligible [71–73]. Following this approach, the pzc of gold and silver single-crystal electrodes was obtained, and the effect of the crystallographic structure of the electrode was systematically investigated [16, 71–73].

The unambiguous thermodynamic definition of the electrode charge (Equation 1.23) is only valid if the transfer of charged particles through the interface is not possible. This situation was denominated as ideally polarizable interphase [74]. In this case, all the charge injected to the interphase through the external circuit is used to build the potential drop between the metal and the solution. The opposite situation is that of the ideally nonpolarizable interphase [75, 76]. In this case, a charged species, common to both sides of the interphase, is in equilibrium. In this case, the corresponding equilibrium condition, the equality of electrochemical potentials at both sides, $\mu_i^{\mathrm{M}} = \mu_i^{\mathrm{S}}$, will impose a relationship between the potential difference, $\Delta_{\mathrm{M}}^{\mathrm{S}}\Phi$ or E, and the chemical potentials of the common species in both sides, μ_i^{M} and μ_i^{S} (Nernst law). In consequence, the potential drop cannot be changed without changing the chemical potential, that is, changing the concentration of the involved species. Under these circumstances, any charge injected to the metal will "leak" into the solution (or vice versa), and the potential difference will not build up. Real interphases correspond always to an intermediate situation between the two ideal descriptions given earlier.

A particular case is obtained when the transfer of charge through the interphase results in the formation of adsorbed species. This case can be thermodynamically described by assigning an (electro)chemical potential to the adsorbed species as if it were a different species from the one in the bulk of the solution. Because the amount of adsorbed species is limited to the surface, in this case the "leaking" of charge is limited, and the interphase can be effectively polarized with the charge remaining in the interphase, although not as true electric or ionic charge but stored in the chemical bonds.

Let us consider the case of a platinum electrode in acid solution with the possible adsorption of hydrogen and the anion, A^-. In this case, the thermodynamic description of the interphase requires the knowledge of four chemical potentials and surface excesses, those of A^- and H^+ and those of the corresponding adsorbed species, H and A. In consequence, the electrocapillary equation for this system will be

$$-d\gamma = \sigma_{\mathrm{M}} dE + \Gamma_{\mathrm{H}^+} d\mu_{\mathrm{H}^+} + \Gamma_{\mathrm{H}} + d\mu_{\mathrm{H}} + \Gamma_{\mathrm{A}^-} d\mu_{\mathrm{A}^-} + \Gamma_{\mathrm{A}} d\mu_{\mathrm{A}} \tag{1.24}$$

However, the different chemical potentials are linked by the two charge transfer equilibrium conditions:

$$\mathrm{H}^+ + \mathrm{e} \rightleftharpoons H \quad \overline{\mu}_{\mathrm{H}^+} + \overline{\mu}_{\mathrm{e}} = \mu_{\mathrm{H}} \tag{1.25}$$

and

$$\mathrm{A}^- \rightleftharpoons \mathrm{A} + \mathrm{e} \quad \overline{\mu}_{\mathrm{A}^-} = \mu_{\mathrm{A}} + \overline{\mu}_{\mathrm{e}} \tag{1.26}$$

Introducing the reference electrode (insensitive to the concentration of H^+ and A^-), we can express the change in the chemical potential of adsorbed species as a function of the electrode potential and the composition of the solution:

$$d\mu_H = d\mu_{H^+} - FdE \tag{1.27}$$

$$d\mu_A = d\mu_{A^-} + FdE \tag{1.28}$$

Introducing these relationships into the electrocapillary equation to remove the dependent variables, we obtain

$$-d\gamma = (\sigma_M - F\Gamma_H + F\Gamma_A)dE + (\Gamma_{H^+} + \Gamma_H)d\mu_{H^+} + (\Gamma_A + \Gamma_{A^-})d\mu_{A^-} \tag{1.29}$$

That can be written as

$$-d\gamma = qdE + \Gamma_{\Sigma H}d\mu_{H^+} + \Gamma_{\Sigma A}d\mu_{A^-} \tag{1.30}$$

where q is the total charge, defined as

$$q = \sigma_M - F\Gamma_H + F\Gamma_A \tag{1.31}$$

and $\Gamma_{\Sigma A}$ and $\Gamma_{\Sigma H}$ are total surface excesses, defined as

$$\Gamma_{\Sigma A} = \Gamma_{A^-} + \Gamma_A \quad \text{and} \quad \Gamma_{\Sigma H} = \Gamma_{H^+} + \Gamma_H \tag{1.32}$$

Equation 1.30 is formally identical to Equation 1.21, only with a different meaning for the variables q, $\Gamma_{\Sigma A}$, and $\Gamma_{\Sigma H}$. The consequence of this derivation is that σ_M, Γ_A, and Γ_H cannot be measured separately by thermodynamic means and only the combination of the three variables given by Equation 1.31 can be obtained. The same happens with the surface excesses Γ_H and Γ_{H^+}: they cannot be determined separately and only the total hydrogen excess $\Gamma_{\sum H}$ can be obtained. Separation of σ_M and q can only be achieved if some extrathermodynamic considerations are assumed [77, 78].

Figure 1.17 illustrates the point discussed earlier. The two interphases sketched in Figure 1.17 A and B are undistinguishable from a macroscopic point of view. They only differ on the microscopic distribution of charges that cannot

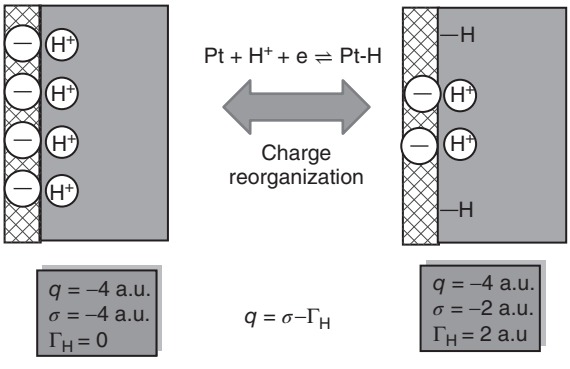

Figure 1.17 Cartoon illustrating the concept of free and total charge on ideally nonpolarizable interphases involving adsorption equilibrium.

be distinguished from a thermodynamic point of view. In fact, we can imagine that interphase B is formed in two steps. First, interphase A is formed, and then, an internal redistribution of charges leads to the formation of covalent bonds. The first step involves the flow of charges through the external circuit (the only that can be measured), while the second step will occur without the detection of external current. The separation of both situations should involve an additional observation that goes beyond the charge measurement. Several structural properties of the interphase, such as dipole orientation under the influence of the electric field, will be sensitive to free charge, σ_M, instead of total charge, q, and therefore will help to disentangle both magnitudes.

The distinction made between total, q, and free charge, σ_M, leads to the related magnitudes – the potential of zero total charge, pztc, and the potential of zero free charge, pzfc, respectively. Also, distinction should be made between the total differential pseudocapacity:

$$C = \left(\frac{\partial q}{\partial E}\right)_{\mu_i} \tag{1.33}$$

and the double-layer differential capacity:

$$C_{dl} = \left(\frac{\partial \sigma}{\partial E}\right)_{\mu_i,\Gamma_i} \tag{1.34}$$

The CO charge displacement discussed earlier turned out to be very helpful for the determination of total charge on platinum electrodes. Under the assumption that no faradaic reaction takes place during CO adsorption, a point that was checked by displacing a iodine monolayer of known coverage [35], the charge flowing during the displacement can be written as [39, 78–80]

$$q_{dis} = q_f^{CO} - q_i \tag{1.35}$$

where q_f^{CO} is the charge on the CO covered surface and q_i is the charge on electrode surface before the introduction of CO at the potential of the experiment. The charge on the CO covered surface can be calculated as

$$q_f^{CO} = \int_{E_{pzc}^{CO}}^{E} C_d^{CO} dE \tag{1.36}$$

where E_{pzc}^{CO} and C_d^{CO} are the pzc of the CO covered surface and its differential capacity, respectively. As a first approximation and considering the very small value of the differential capacity C_d^{CO}, the charge on the CO covered surface can be neglected, and the displaced charge considered as equal to the total charge present on the initial surface at the potential of the experiment [39]. The value of E_{pzc}^{CO} was first estimated from work function measurements of the CO-covered surface [81] and later measured with the immersion method for Pt(111) in 0.1 M $HClO_4$ [82]. With this value of E_{pzc}^{CO}, an estimation for the residual charge after the CO displacement can be obtained, resulting around $-13\,\mu C\,cm^{-2}$ at 0.1 V RHE. The negative sign is the consequence of the very high value of the E_{pzc}^{CO}, which is estimated to be around 1 V RHE for Pt(111). When the total charge is known at a one given

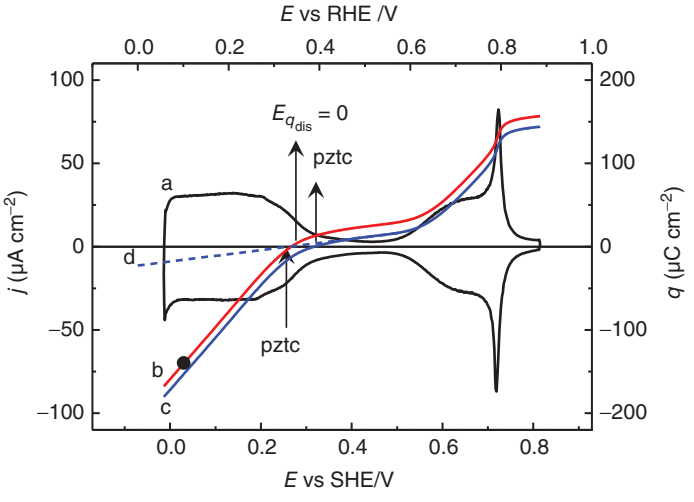

Figure 1.18 Illustration of the procedure for the determination of the charge versus potential curve from the combination of CO charge displacement and the integration of the voltammogram for Pt(111) in 0.1 M $HClO_4$. (a) Cyclic voltammogram 50 mV s^{-1}. (b) Uncorrected charges obtained neglecting the residual charge on the CO-covered surface. (c) Charges corrected considering $E_{pzc}^{CO} = 1$ V. (d) Free charge extrapolated considering constant value of the double-layer differential capacity. The circle represents the opposite of the displaced charge at 0.1 V RHE. (Adapted from Rizo 2015 [78]. Reproduced with permission of Elsevier.)

potential, it can be combined with the integration of the voltammogram to obtain a complete curve of the charge as a function of the potential according to

$$q(E) = (q_f^{CO}(E_{dis}) - q_{dis}(E_{dis})) + \int_{E_{dis}}^{E} \frac{j}{\nu} dE \tag{1.37}$$

where E_{dis} is the potential of the displacement experiment and j and ν are the voltammetric current and the scan rate (with sign), respectively. This is illustrated in Figure 1.18.

1.5.1 Total Charge Curves in Coulometric Analysis

The knowledge of total charge curves obtained from CO charge displacement has a very important application in the correct determination of coverage of adsorbed species from coulometric measurement. During the stripping of an irreversibly adsorbed monolayer, charge flowing through the external circuit is a complex measure that includes multiple contributions. The simplest case includes the stoichiometry of the reaction for the adsorbate elimination and the restoration of the double-layer properties at the final potential. Calculation of the coverage needs to separate these contributions to the overall charge to identify the portion that is truly associated with the faradaic process.

The stripping of an adsorbate usually leads to strong changes in the properties of the interphase, resulting in a flow of (pseudo)capacitive current that adds to the true faradaic charge. For platinum group metals, where hydrogen and anion adsorptions add to the purely capacitive processes, neglecting these contributions can lead to large errors.

To illustrate these issues, it helps to consider some examples where the coverage is independently known from measurements other than charge determinations. One of such examples is the CO adlayers on well-defined platinum surfaces. The system has been extensively studied by a multiplicity of techniques given its importance in the understanding of the oxidation of small organic molecules. STM [83] and X-ray diffraction [84] studies provided structural information that allows the accurate calculation of coverage values at different potentials. Different adlayer structures were found depending on the potential and on whether CO is present or not in the solution. (2×2)-3CO and $(\sqrt{19}\times\sqrt{19})$R23.4-13CO structures with coverages of 0.75 and 0.68, respectively, were found for CO in solution, while a $(\sqrt{7}\times\sqrt{7})$R19.1-4CO structure was found in the absence of CO in solution [83]. Vibrational spectroscopy measurements complement this information and supports the persistence of the (2×2)-3CO structure even after removing CO from solution [85]. In addition, infrared spectroscopic measurements allowed, after careful calibration, calculation of coverages. Such measurements consistently give a value of coverage around 0.6 or 0.7 for CO adsorbed on Pt(111). On the other hand, voltammetric CO stripping can be achieved in a well-defined peak by sweeping the potential of the electrode to values sufficiently high, according to the balanced equation

$$CO + H_2O \rightarrow CO_2 + 2H^+ + 2e \tag{1.38}$$

This gives a value of voltammetric stripping charge of 437 $\mu C\,cm^{-2}$ [86]. This charge can be used to calculate an apparent charge transfer number as

$$l = \frac{q_{CO}}{F\Gamma_{CO}} = \frac{q_{CO}}{\theta q_{111}} \tag{1.39}$$

where q_{CO} is the overall charge measured in the stripping and q_{111} is the nominal value of the charge corresponding to one electron per platinum atom on the (111) surface. Application of this equation would give a value for l around 3, significantly higher than the value of 2 expected from Equation 1.11. The reason for this abnormally high value of l is that, associated with CO removal, there is a charge flowing due to the recovery of the double layer, in particular, to anion adsorption on the surface sites that become available after CO oxidation [86]:

$$q^{raw} = \left[q(E_+) - q^{CO}(E_-)\right] + q^{far} \tag{1.40}$$

where q^{raw} is the overall charge including both the double layer and faradaic processes; $q(E_+)$ and $q^{CO}(E_-)$ are the total charges at the interphase at the end and at the beginning of the potential sweep, respectively; and q^{far} is the true faradaic charge due to CO oxidation.

While $q^{CO}(E_-)$, the charge on the CO covered surface, is rather small, as discussed earlier [82], $q(E_+)$ corresponds to the charge in the absence of CO and

therefore represents a significant contribution. This charge can be read directly from the charge versus potential curve, obtained as described earlier. For Pt(111) this charge amounts to 129 μC cm^{-2}, when E_+ equals 1.0 V, and represents a significant fraction of the total 437 μC cm^{-2} recorded during CO oxidation. The separation of charges into double layer and faradaic is formal since only the overall charge can be measured, however, to obtain the correct coverage – either the correction described earlier is done or the formal apparent value of charge transfer given in Equation 1.39 is used.

Careful comparison of Equations 1.40 and 1.37, taking $E_- = E_{dis}$ and therefore $q^{CO}(E_-) = q_f^{CO}$, shows that these terms cancel and the correction becomes exact even if $q^{CO}(E_-)$ is not known. This is a particular case, since the molecule used for the charge displacement is the same molecule in which coverage is being calculated. This has been demonstrated considering a closed cycle that includes the steps of CO dosage, voltammetric stripping, and potential scan to the initial potential value. In this cycle, since final and initial situations are identical, the only charge involved corresponds to the faradaic oxidation of the CO adlayer [87].

The CO displacement experiment has been used numerous times for the estimation of total charges in different situations. In general good agreement has been found between the displaced charges for different anions such as chloride and bromide [36] and the coverages calculated from a thermodynamic method [88, 89].

A similar situation is encountered for reductive stripping of NO adlayers. NO adsorbs irreversibly on platinum and remains adsorbed even after transfer of the electrode to a NO-free solution. Under these conditions, NO can be reductively desorbed from the electrode according to the chemical equation [90, 91]

$$NO + 6H^+ + 5e \rightarrow NH_4^+ + H_2O \tag{1.41}$$

Similarly to what has been described earlier for CO, after stripping of the adlayer, the charge value characteristic of the clean platinum–solution interphase is recovered. Since in this case, the reductive stripping ends at a potential where the platinum is normally covered with hydrogen, the charge due to the recovery of the hydrogen adlayer has to be considered now in addition to the capacitive charge of the interphase. As before, this can be calculated from the CO charge displacement experiment, according to Equation 1.37. Let us consider the Pt(100)-NO as example [90]. In this case, the reductive stripping of the NO adlayer involves a charge around 700 μC cm^{-2}. A significant amount of this charge corresponds to the recovery of the clean interphase at 0.06 V, including hydrogen readsorption, amounting to 200 μC cm^{-2}. Therefore, the NO coverage can be calculated as

$$\theta = \frac{q^{raw} - q_{E_-}}{nq_{100}} \tag{1.42}$$

where q^{raw} is the overall charge integrated in the voltammetric sweep from E_i to E_-, q_{E-} is the total charge at the lower limit of the voltammetric sweep, and q_{100} is the charge corresponding to one electron per platinum atom on the (100) surface. In this particular example, a coverage of 0.5 is obtained in agreement with data measured in UHV [90].

1.5.2
Model for the Estimation of the Potential of Zero Free Charge

The particular case of Pt(111) in perchloric acid allows further analysis, taking advantage of the fact that hydrogen and hydroxyl adsorption regions are well separated. If we assume that the region between 0.4 and 0.6 V (traditionally the so-called double-layer region) corresponds to purely capacitive behavior, without faradaic adsorption reactions, $\Gamma_H = \Gamma_{OH} = 0$ and Equation 1.31 reduces to

$$q = \sigma_M \quad \text{in the double-layer region} \tag{1.43}$$

This provides a value that could be combined with the integration of the double-layer differential capacity, as defined in Equation 1.34 (if known), to calculate a curve that relates σ_M as a function of *E*. As a first approximation, the differential capacity of the double layer was taken as constant and the free charge linearly extrapolated outside the double-layer region to get an estimation of the position of the pzfc [79]. The procedure is exemplified in Figure 1.18 where it can be clearly seen that the pzfc lies at potentials slightly more negative than the pztc.

A refined analysis used values of the double-layer differential capacity extracted from a thermodynamic analysis [77, 87]. While the position of the pzfc changes slightly with the use of the better estimation of the differential capacity, the conclusions, particularly about the location of the pzfc negative to the pztc, do not change. In fact, this conclusion was previously obtained for polycrystalline platinum by other methods [75].

Following the same approach discussed in previous paragraphs, the effect of pH on the location of the pztc and pzfc has been investigated more recently [78, 92]. As the pH becomes more alkaline, the location of the pztc displaces from the hydrogen region into the hydroxyl region. In fact, position of the pztc is rather insensitive to the pH, while hydrogen and hydroxyl adsorption processes shift with pH nearly 0.059 V per pH unit. One consequence of this shift is that the relative position of pztc and pzfc changes, and for pH > 4, pzfc > pztc. At pH around 3, the pztc lies exactly in the double-layer region and, therefore, pztc and pzfc coincide [92].

1.5.3
Applications of Electrocapillary Equation

The electrocapillary equation described earlier, Equation 1.26, can be used to obtain thermodynamic information about the hydrogen and anion adsorption processes. This analysis parallels the classical thermodynamics studies of the electrified interphase on mercury electrodes. The application of the electrocapillary equation to solid electrodes was pioneered by Lipkowski's group, initially applied to gold electrodes [93–96]. While the application of this equation to solid electrodes has been criticized because in this case elastic strain should also be considered, careful consideration of the limited available data indicates that this term is reasonably negligible [97]. The application of this analysis to platinum

electrodes requires the introduction of the notion of total charge, as described earlier [77, 88, 89, 98–104]. According to Equation 1.30, the coverage of an anion is given by

$$\Gamma = -\left(\frac{\partial \gamma}{\partial \mu_{A^-}}\right)_E \tag{1.44}$$

where surface tension can be calculated from

$$\gamma - \gamma^* = -\int_{E^*}^{E} q\, dE \tag{1.45}$$

where γ^* is the surface tension at the lower limit of integration, E^*. The analysis starts with a set of voltammograms measured at different concentrations of the anion in solution. Integration of the voltammograms leads to a set of charge curves at different concentrations. This integration would require information from CO displacement experiments to account for the integration constant. However, for the application of Equation 1.44, these additional measurements can be avoided if the lower limit of integration is chosen such as the integration constant is independent of the concentration of the anion. In this case

$$\Delta q = q - q^* = \int_{E^*}^{E} \frac{j}{\nu}\, dE \tag{1.46}$$

and

$$\gamma - \gamma^* = -\int_{E^*}^{E} \Delta q\, dE - \int_{E^*}^{E} q^*\, dE \tag{1.47}$$

With a correct selection of E^*, the second term will be independent of anion concentration and will disappear when the derivation in Equation 1.44 is done. The same happens with the unknown value of γ^*. When dealing with anion adsorption, E^* should be chosen low enough so that the interphase becomes independent of anion in solution [88, 89, 98]. The relative position of the charge curves obtained from the integration of the voltammogram at different concentrations is adjusted so all of them converge at low potential values. Moreover, if the integration constant is known for one concentration from a CO displacement, by adjusting the relative position of all the curves, total charge will be known for all concentrations without the necessity of measuring the displaced charge in each composition. To avoid the necessity of accounting for the activity coefficient in the definition of μ_{A^-}, solutions with a constant ionic strength and excess of supporting electrolyte are used [68]. Under such condition, the activity coefficient will be independent of anion concentration, and derivatives against (ln a) and against (ln c) become equal.

With this approach, surface coverage of the anion can be obtained as a function of anion concentration. However, it has been shown that better results are obtained if, before the analysis, a Legendre transform of the electrocapillary equation is taken to change the independent variable from potential to charge [98]:

$$d\xi = E dq - \Gamma d\mu \tag{1.48}$$

where ξ is called the *Parsons function*. To obtain ξ, the potential should be integrated as a function of charge for each concentration:

$$\xi - \xi^* = \int_{Q^*}^{Q} E\,dq \tag{1.49}$$

As before, Q^* is selected at a potential value where no adsorption of the anion takes place. Again, there is no need to know the true values of total charge, with their relative values being sufficient:

$$\xi - \xi^* = \int_{q^*}^{q} E dq = \int_{0}^{\Delta q} E d\Delta q \tag{1.50}$$

Finally, the surface excesses can be determined from the following derivative:

$$\Gamma = -\left(\frac{\partial \xi}{\partial \mu}\right)_q \tag{1.51}$$

With this approach, surface excess is obtained as a function of total charge. Finally, surface excess can be plotted as a function of potential using the knowledge of the curves charge versus potential.

Figure 1.19 compares surface excesses of several anions adsorbed on Pt(111). The strength of the adsorption follows the order OH < SO_4 < Cl < Br, as deduced from the shift to lower potentials of the onset of adsorption. Chloride and OH reach similar maximum coverages, around $\theta = 0.5$, while bromide coverage is lower, reflecting the bigger size of this anion. Finally, SO_4 coverage is much lower, reflecting the formation of a rather open adlayer structure, as observed with STM [42, 43]. Other magnitudes accessible with this thermodynamic analysis are charge numbers and Gibbs adsorption energies [88, 89, 102].

1.6 The Laser-Induced Temperature Jump Method and the Potential of Maximum Entropy

One technique that has proved very valuable in providing additional interfacial information is the laser-induced temperature jump method [105–113]. In this technique, the coulostatic (open-circuit) potential transients that take place in response to a sudden change of the temperature are used to extract thermodynamic and kinetic information about the interphase. The fast increase of the temperature is achieved by using irradiation with a pulsed high-power laser source. The second harmonic of an Nd:YAG laser provides green light (532 nm) that can be used for this purpose. The light is partially reflected at the metallic surface and partially absorbed. The fraction of light that is absorbed is almost immediately converted into heat, increasing the temperature of the interphase. Pulses of laser light of 1–3 mJ per pulse and pulse duration of 5–10 ns allow increasing the temperature of the interphase in the nanosecond timescale by 10–30° [108]. In this methodology, the change of the open-circuit potential in response to the

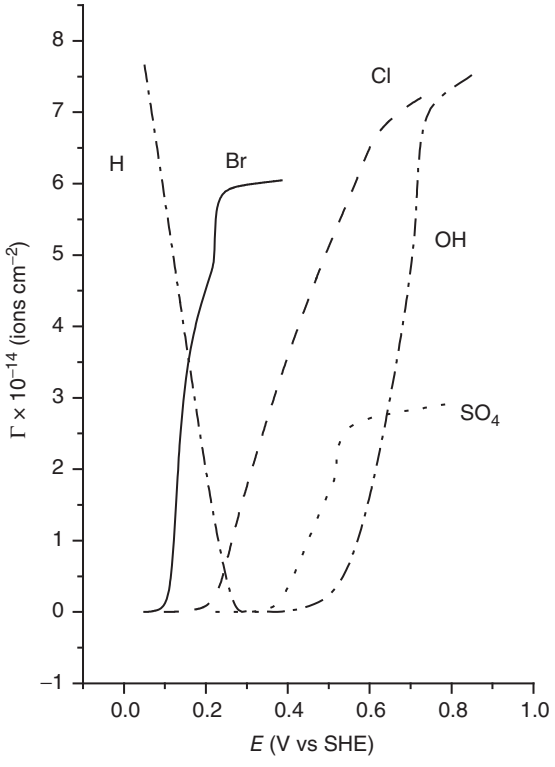

Figure 1.19 Comparison of surface excesses of bromide (solid line), chloride (dashed line), and sulfate (dotted line) in 0.1 M $HClO_4$ with 10^{-3} M of the anion. Hydrogen and OH surface excesses in 0.1 M $HClO_4$ are also included for comparison. (Garcia-Araez 2006 [89]. Reproduced with permission of Elsevier.)

change of the temperature is recorded in the submicrosecond time scale. While the temperature change cannot be measured, it can be calculated from a very simple model of heat transfer [108]. For measuring times sufficiently longer than the duration of the laser pulse, the temperature relaxes due to heat diffusion following the expression:

$$\Delta T = \frac{1}{2}\Delta T_0 \sqrt{\frac{t_0}{t}} \tag{1.52}$$

If the response of the interphase is sufficiently fast so the system can be considered in equilibrium, the recorded open-circuit potential transient can be used to calculate the thermal coefficient $(\partial \Delta_S^M \phi / \partial T)_{q,p,a_i}$. Note that, in this experiment, the temperature of the reference electrode is not changed, and therefore, the temperature coefficient that is determined is that of a nonisothermal cell. For this reason, we can approximate $(\partial \Delta_S^M \phi / \partial T)_{q,p,a_i}$ to $(\partial E / \partial T)_{q,p,a_i}$. In reality, a small thermodiffusion potential [114] will arise as a consequence of the different

temperatures in the solution, but this is usually very small [107]. By neglecting the thermodiffusion potential, we can write

$$\Delta E = \left(\frac{\partial \Delta_S^M \phi}{\partial T}\right)_{q,p,a_i} \Delta T = \frac{1}{2}\Delta T_0 \sqrt{\frac{t_0}{t}} \left(\frac{\partial \Delta_S^M \phi}{\partial T}\right)_{q,p,a_i} \tag{1.53}$$

Therefore, the temperature relaxation should decay proportional to the inverse of $\sqrt{t}$, and the proportionality constant allows the calculation of the thermal coefficient of the potential drop at interphase. Although the potential change is measured under open-circuit conditions (this ensures the coulostatic condition, i.e., constant charge, in the derivative) for an ideally polarizable interphase, potential of the electrode can be changed, and the coefficient measured as a function of the potential. For this purpose, a system of switches allows synchronization of the potentiostat and the T-jump experiment, disconnecting the potentiostat just before firing the laser.

The reader might be wondering what is the advantage of using a sophisticated setup that includes a relatively expensive high-power laser to measure a thermal coefficient that can be measured by simply using a thermostated cell. The answer is in the time scale of the measurements. By doing the temperature jump sufficiently fast, double-layer response can be decoupled from adsorption processes, normally much slower. This can be seen in Figure 1.20, where the coulostatic potential transients for a Pt(111) in solution of different pH are measured in the hydrogen potential region. In the most acidic solution, a bipolar shape of the transient clearly shows that Equation 1.53 is not satisfied in this case, since this equation predicts a monotonous decay and is therefore clearly incompatible with the shape obtained in this case. The reason for this behavior is the contribution of hydrogen adsorption to the change of the potential. Since hydrogen adsorption implies charge transfer, perturbation of the hydrogen equilibrium under open-circuit conditions implies a displacement of the electrode potential. From the shape of the transient under these conditions, it has been possible to get an estimate of the rate constant for the hydrogen adsorption process. However, what is more important is that as the pH increases, the rate of hydrogen adsorption decreases and the potential transient becomes monotonous.

Therefore, by carefully selecting the conditions of the experiments, in this case, the pH of the solution, the T-jump measurements allow determination of the thermal coefficient of the double layer, under condition of constant coverage of adsorbed species, $\left(\partial \Delta_S^M \phi / \partial T\right)_{q,p,a_i,\Gamma_i}$.

The different potential transient obtained for Pt(111) at different potentials are depicted in Figure 1.21. The most interesting observation in this figure is the change of sign of the potential transients depending on the electrode potential. Positive transients are obtained at the higher potentials, while negative transients are obtained at the lower potentials. This indicates a change of sign of the thermal coefficient $\left(\partial \Delta_S^M \phi / \partial T\right)_{q,p,a_i,\Gamma_i}$. The main contribution to this coefficient comes from the perturbation of the water dipoles at the interphase as the temperature increases. Other contributions different from the dipolar term to the thermal

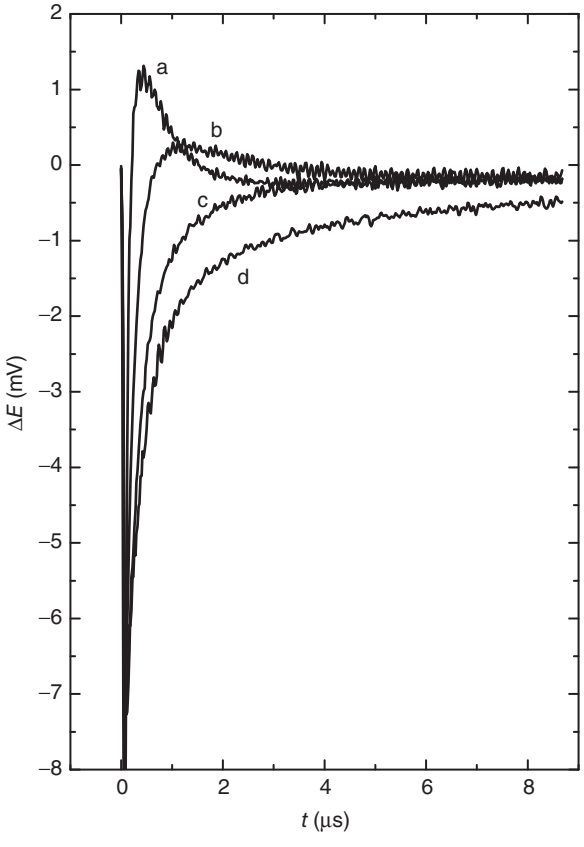

Figure 1.20 Laser-induced potential transients for Pt(111) at $E = 0.15$ V in $(0.1 - x)$ M $KClO_4 + x$M $HClO_4$, where x equals (a) 0.1, (b) 10^{-2}, (c) 10^{-3}, and (d) 10^{-4}. (Adapted from Climent 2002 [107]. Reproduced with permission of American Chemical Society.)

coefficient come from the effect of temperature on the spillover of electrons and the diffuse layer [105–107, 110, 115]. The first can be estimated from the work function of the surface and the second from the Gouy–Chapman model, resulting in the effect of the temperature on the dipolar term being the main contribution [107, 110, 115]. For low potentials, the metal will be negatively charged and water dipoles will be oriented with the hydrogen end closer to the surface. This results in a positive dipolar contribution to the potential drop at the interphase. Increasing the temperature will decrease the order in the water dipole layer, resulting in the decrease of the positive dipolar contribution to the potential and, hence, the negative transient. The opposite takes place at high potentials, with the electrode positively charged attracting the oxygen end of water dipoles and resulting in a negative contribution to the potential drop at the interphase. Decreasing this negative contribution results in a positive potential transient. The most significant point is the potential where the transient is zero.

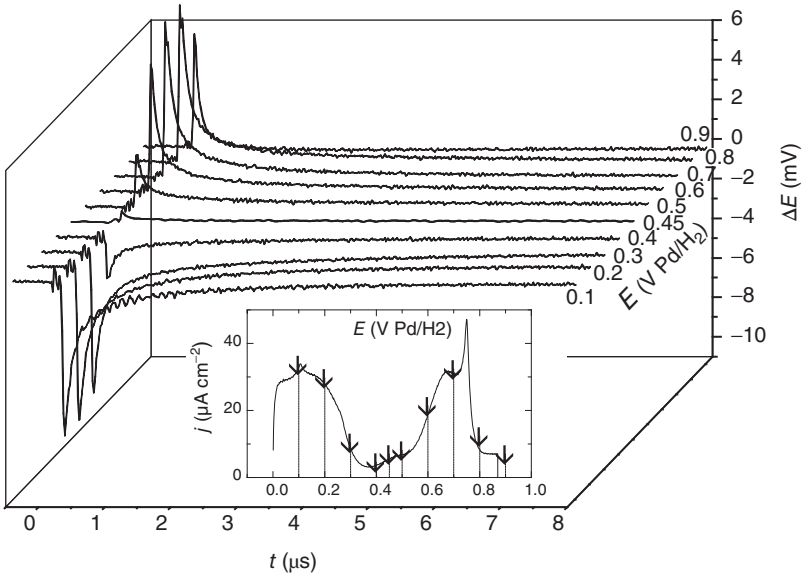

Figure 1.21 Laser-induced potential transients for the Pt(111) electrode in 0.1 M $KClO_4 + 10^{-3}$ M $HClO_4$ at different potentials as indicated. (The Pd/H_2 reference electrode is shifted 50 mV with respect to the RHE). (Climent 2002 [107]. Reproduced with permission of American Chemical Society.)

This point corresponds to the potential where dipolar contribution is zero, resulting in a negligible change of potential as the temperature is increased. The orientation of water dipoles is mainly governed by the sign of the free charge at the interphase. A small difference between the potential of zero transient and the pzfc can be expected since a chemical interaction between water and the surface will favor the orientation of the water with the oxygen closer to the surface in the absence of an electric field. However, this difference is small, and therefore determination of the potential of zero transient gives a good estimation of the pzfc. The reader should remember that we claimed earlier that pzfc is not accessible purely by thermodynamic measurements. Here, the magnitude became accessible by decreasing the time scale of the measurement, therefore decoupling the adsorption processes from the purely capacitive processes according to their different time scales. The other way how this separation could be achieved is by performing high-frequency impedance measurements.

Thermodynamic considerations based on the electrocapillary equation lead to the following equation, resulting from the equality of cross differentials [107, 108, 115]:

$$\left(\frac{\partial \Delta S_{\mathrm{dl}}}{\partial q}\right)_{T,p,a_i} = -\left(\frac{\partial \Delta_{\mathrm{S}}^{\mathrm{M}} \phi}{\partial T}\right)_{q,p,a_i,\Gamma_i} \tag{1.54}$$

where q is the total charge, $\Delta\phi$ is the potential difference at the interphase, and ΔS_{dl} is the entropy of formation of the interphase, defined as the difference between the entropy of the components of the interphase when they are forming it and when they are present in the bulk of their respective phases. Then, the entropy of formation of the interphase can be determined, up to an integration constant, by integrating the thermal coefficient as a function of the total charge. According to this expression, the potential of zero transient can be identified with a maximum (or a minimum) in the curve ΔS_{dl} as a function of charge (it will be a maximum if the thermal coefficient changes from negative to positive). Therefore, the potential of zero transient can be also called *potential of maximum entropy (pme)*.

Figure 1.22 shows a comparison of the Potential of maximum entropy (pme) and the pztc for the three basal planes of platinum in solutions of perchloric acid and perchlorate of different pH. For Pt(111), pztc and pme are very similar. As previously discussed for Pt(111) in the absence of anion adsorption, pztc lies in the double-layer region, and therefore, pztc and pzfc are very similar. Therefore, in this case, pme, pztc, and pzfc are very close. For Pt(110) and Pt(100), pme is located more negative than the pztc. For these surfaces, the pztc lies in the hydrogen adsorption region. Therefore, at the pztc, a positive value of free charge is

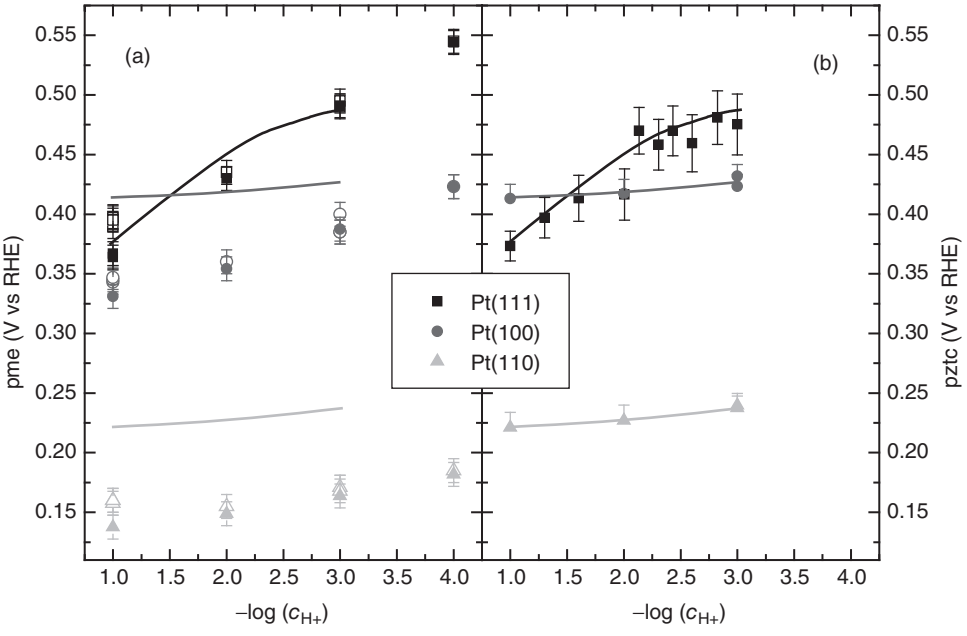

Figure 1.22 Values of (a) pme's, uncorrected (open symbols) and corrected (filled symbols) from the thermodiffusion potential, and (b) pztc's for Pt(111), Pt(100), and Pt(110) electrodes in $(0.1 - x)$ M $KClO_4 + x$M $HClO_4$ solutions. Lines are drawn to indicate the tendencies of pztc values, and they are reproduced in the left figure in order to facilitate the comparison with pme values. (Garcia-Araez 2009 [112]. Reproduced with permission of American Chemical Society.)

necessary to compensate the negative contribution from adsorbed hydrogen. For this reason, the pzfc lies more negative than the pztc explaining the relative position between pme and pztc.

These measurements have been extended to other metal surfaces and other electrolyte solutions. The results obtained with gold electrodes give support to the previous interpretation since they are in good agreement with conventional measurements of the thermal coefficient using a thermostated cell [108]. More recently the laser-induced T-jump method has been applied to study the interphase between single-crystal surfaces and ionic liquid solutions [158].

1.7 Electrocatalytic Studies with Single-Crystal Electrodes

The extensive knowledge gained with the study of single-crystal electrodes about the influence of surface structure on the electrochemical properties of platinum has proved invaluable to understand its electrocatalytic properties regarding many reactions of technical interest. Parameters such as interaction of intermediates with the surface, specific adsorption of anions and other "spectator" species, potential of zero (total and free) charge, and orientation of water molecules at the interphase are all key in the understanding of the electrocatalytic phenomena. In the following we illustrate this approach with a couple of examples, such as carbon monoxide adsorption and oxidation, and oxygen reduction.

1.7.1 Carbon Monoxide on Platinum

Carbon monoxide adsorption on well-defined metallic surfaces has been a benchmark system in both UHV studies and surface electrochemistry [83, 85, 116–127]. Carbon monoxide adsorbs very strongly on all platinum surfaces also in aqueous environment. In addition to the fundamental interest on this molecule, these studies have a strong relevance in electrocatalysis since CO is the most common poison formed during the oxidation of small organic molecules [128]. Improving oxidation rate for CO is a way to improve the performance of catalysts for the oxidation of fuel such as methanol, ethanol, or formic acid.

One should distinguish two approaches for the study of CO oxidation: stripping of CO adlayers in the absence of CO in solution and CO oxidation from CO-saturated solutions. In the first one, the oxidation is limited to species on the surface, and a peak is obtained as described previously. When CO is present in solution, after the oxidation of the surface molecules, new CO molecules will occupy the freed sites and the reaction will proceed. In this case, rate of reaction will be mass transport limited, and therefore it will be convenient to use rotating disk configuration. The following discussion will focus on the oxidation of CO adlayers in the absence of CO in solution.

There is widespread consensus that oxidation of carbon monoxide proceeds through a Langmuir–Hinshelwood mechanism [129–131]. In this mechanism the rate-determining step involves the reaction between two adsorbed species, in this case, adsorbed CO and adsorbed OH:

$$Pt + H_2O \rightleftharpoons Pt\text{-}OH + H^+ + e \tag{1.55}$$

$$Pt\text{-}CO + Pt\text{-}OH \rightarrow Pt\text{-}COOH \tag{1.56}$$

$$Pt\text{-}COOH \rightarrow Pt + CO_2 + H^+ + e \tag{1.57}$$

Dependence of reaction rate on surface coverages and electrode potential depends markedly on the surface mobility of adsorbed species, with two extreme situations [132, 133]. For a large mobility, a perfect mixing of OH and CO is attained, and the mean field approximation holds. Under this approximation, current is proportional to the average coverage of both adsorbed species:

$$j = 2Fk\theta_{CO}\theta_{OH} \tag{1.58}$$

In addition, it is usually accepted that OH adsorption is in equilibrium, and therefore its coverage is proportional to the number of free sites $(1 - \theta_{CO})$. In this case, the expression can be replaced by

$$j = 2Fk'\theta_{CO}(1 - \theta_{CO}) \tag{1.59}$$

Under these assumptions, it is easy to find an analytical expression relating the current with the electrode potential or time for linear sweep voltammetry or chronoamperometric experiments, respectively [130].

The other extreme situation is when mobility of adsorbed species is very low. This leads to the nucleation and growth model. In this case, reaction will start at some active sites or points on the surface containing adsorbed OH. As CO is oxidized around these active sites, OH islands will grow on the free platinum sites resulting from CO oxidation. Within this case, two additional limiting situations can be differentiated, instantaneous and progressive nucleation, depending on whether active sites are present from the beginning or are being created during the course of the reaction [134].

Since the rate of the oxidation of CO is very sensitive to the nature of the adsorption site, it is of fundamental importance to study this reaction using well-defined electrode surface. Use of stepped surfaces has proved of great value to discriminate between the previous situations, allowing the calculation of kinetic parameters [129, 135]. Chronoamperometic experiments in acidic media with Pt(111) and stepped surfaces demonstrated the inadequacy of nucleation and growth models to fit the time dependence of the current [129, 130]. On the other hand, mean field model resulting from the integration of Equation 1.59 gave satisfactory fits for all potentials and stepped surfaces, reaching the conclusion that surface mobility of CO in acidic media is sufficiently high. Moreover, the rate constant for CO oxidation measured for stepped surfaces with (111) terraces shows a linear dependence on the fraction of step atoms on the surface, supporting the idea that step atoms are the active sites for CO oxidation and CO on the terrace diffuses to step sites

before they can be oxidized [129]. One interesting conclusion is that extrapolation of rate constant for CO oxidation to zero step density gives a negligible value, suggesting that a perfect (111) surface would be unable to oxidize CO. This is a good example showing how controlled introduction of steps on the (111) surface allows, by extrapolation, to obtain parameters for the ideal surface, which is, otherwise, unattainable in a real experiment. Spectroscopic results indicate that the bottom of the step and not the step edges are active for CO oxidation [135]. This activity results from the enhanced adsorption of oxygenated species at the bottom of the step, resulting from the excess positive charge consequence of the Smoluchowski effect [136]. On the other hand, CO adsorbed at the step edge (top of the step) is less reactive due to the extra stability resulting from the enhanced backdonation from the low-coordinated Pt atoms. [135]

The potential dependence of the rate constant allows calculation of an apparent Tafel slope for all stepped $n(111)\times(111)$ surfaces around (80 ± 8) mV dec^{-1}. This value, relatively close to 60 mV dec^{-1}, is consistent with the existence of a chemical process as limiting step in the mechanism [129].

The mean oxidation peak is usually preceded with a prewave [137, 138]. Also, chronoamperometric experiments have shown the existence of a plateau region of constant current until the main oxidation peak starts [129, 130]. This prewave has been assigned to the oxidation of CO near defect sites without freeing platinum sites and therefore without increase of the current [129, 130, 137, 138]. This is possible since complete blockage of the surface can be attained with a broad range of CO coverages from 0.6 to 0.75, a fact that reflects the possible existence of different structures, such as the $\sqrt{7}\times\sqrt{7}$ or (2×2)-3C with different maximum coverage.

Mobility of CO depends strongly on parameters such as the electrode potential or pH of the solution. In a recent experiment, CO adsorption on a Pt(S)-[$n(111)\times(100)$] stepped surface from a dilute solution of this gas was monitored by continuously recording the voltammogram in the low potential region where oxidation does not take place [139]. The result was that CO adsorption takes place initially with no preference for terrace or step sites. However, allowing a purging time with Ar for several minutes leads to a restructuring of the CO adlayer with preferential accumulation on step sites. This points toward a low mobility of CO, since long time in the scale of minutes is required for diffusion from terrace to step sites. These results contrast with the satisfactory application of mean field equations to model CO oxidation. The only way to conciliate both results is to consider that CO mobility depends strongly on potential, being sufficiently fast at the high potentials required for its oxidation but slow at low potentials.

This explanation agrees also with the results obtained at higher pHs. In acidic solutions CO oxidation on stepped surfaces by linear sweep voltammetry exhibits only one peak [140]. This agrees again with the high mobility previously mentioned. In this case, although the reaction starts on steps, the high rate of diffusion allows a fast mixing of species on the surface, therefore satisfying the mean field approximation. As step density is increased, the voltammetric peak shifts to lower potentials (linear voltammetry) without splitting. However in alkaline

solutions, several voltammetric peaks are resolved, corresponding to terrace and steps, clearly indicating a much lower mobility in this case [141]. This low mobility is explained considering that higher pH implies oxidation of CO at lower potentials (same potentials in the RHE scale imply lower potentials in an absolute reference scale). Lower electrode potentials stabilize CO adsorption by stronger backdonation. This is a well-known fact from spectroscopic experiments [116].

1.7.2 Oxygen Reduction

The oxygen reduction reaction (ORR) is one of the most important reactions in electrochemistry. Oxygen is the most common ultimate electron acceptor in aerobic forms of life, and therefore ORR is omnipresent in biological reactions. ORR also appears in corrosion processes, and, in this sense, its study has strong technological implications. Most importantly for the subject of the present review, ORR is the preferred cathode reaction for fuel cells. In this context, ORR has been investigated on Pt and different Pt alloys with the aim of improving the performance of fuel cells. It has been unequivocally demonstrated that this reaction is sensitive to the crystallographic structure of the electrode surface, and therefore most of the research on the catalysis of this reaction, especially that at a fundamental level, involves the use of single crystals.

The ORR involves four electrons and therefore takes place through a rather complex mechanism. It is generally accepted that the initial step is a first electron transfer resulting in the formation of adsorbed O_2^- [142–149]. This is followed by a second electron transfer and one or two proton transfers to form adsorbed peroxide species. The latter can desorb to form hydrogen peroxide or can be further reduced to water. Finally, the intermediate hydrogen peroxide formed in solution can diffuse to the bulk or be reduced to water, depending on the potential and nature of the electrode. The following scheme summarizes these steps:

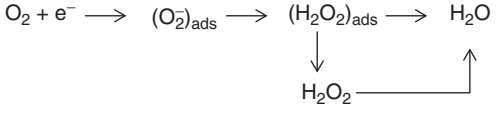

(1.60)

Since O_2 solubility in water solutions is low and achieved currents can be relatively high, the reaction will be soon controlled by mass transport, and extraction of kinetic parameters can be hampered by the limited rate of diffusion. To avoid this problem, the proper experimental setup to study the ORR involves the use of a rotating disk electrode (RDE). True RDE configuration using single crystal is difficult to achieve, mainly because of the necessity of a flame annealing step to decontaminate the surface which is incompatible with a polymer covering the sides of the electrode. For this reason, most of the experiments in this field have been done in the hanging meniscus configuration. The most notable exception to this statement is the work of Markovic, who devised a method of embedding the electrode in a Teflon cylinder after flame annealing while reasonably preserving

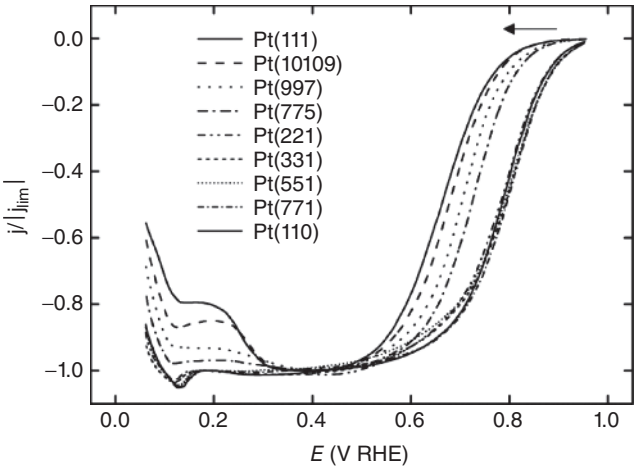

Figure 1.23 Linear sweep voltammograms for oxygen reduction on selected Pt-stepped electrodes in the [1$\bar{1}$0] in 0.5 M H_2SO_4. Scan rate: 50 mV s^{-1}. Rotation rate: 1600 rpm. (Kuzume 2007 [142]. Reproduced with permission of Elsevier.)

the cleanliness of the surface [143–145, 150, 151]. While cleanliness and quality of the surface in this case is lower than that achieved for small bead electrodes used in the hanging meniscus configuration, still interesting information can obtained with this methodology, especially when a ring disk configuration is used, since this allows the detection of the intermediates (hydrogen peroxide) formed in the course of the reaction.

Figure 1.23 shows linear sweep voltammograms for ORR on platinum stepped surfaces in the [1$\bar{1}$0] zone in sulfuric acid solution. The (111) is the surface with the lowest activity. In consequence, the curve appears at lower potential (higher overpotentials). Between 0.5 and 0.8 V RHE, the current has a kinetic component, while between 0.35 and 0.5 V a plateau is achieved corresponding to the maximum possible current as limited by the rate of O_2 mass transport. One of the most remarkable features of the curve for Pt(111) is the decrease of current for potentials below 0.3 V. The onset for this decrease coincides with the beginning of the hydrogen adsorption on this surface. Ring disk experiments demonstrate that this decrease is accompanied by an increase in the amount of produced hydrogen peroxide [143]. To explain this effect, it is usually accepted that hydrogen adsorption limits the availability of the surface sites for the adsorption of oxygen. The consequence is that the adsorbed intermediate cannot coordinate in the bridge configuration necessary to weaken the O–O bond. Conversely, a linear coordination with only one O interacting with the surface leads to the formation of hydrogen peroxide that is desorbed to the solution before completing the reduction to water. Some of this H_2O_2 can still be reduced at potentials above 0.13 V. This explains two further observations [142]: (i) there are two drops in the current, between 0.3 and 0.13 and below 0.13 V and (ii) the current drop at low potentials increases with the rotation rate. The first point is explained considering that

below 0.13 V H_2O_2 reduction is also inhibited by the adsorbed hydrogen, causing the second drop in the current. The second observation results from the effect of increasing rotation rate on the transport of the produced H_2O_2 away from the surface, therefore decreasing the chance of this intermediate being reduced to water.

Interestingly, the inhibiting effect of adsorbed hydrogen is also sensitive to the crystallographic structure, and the introduction of (110) steps significantly decreases it. Ring disk experiments have shown that the amount of H_2O_2 produced in the lower limit of potentials goes in the order (111) > (100) > (110) [143, 145]. The lowest effect of hydrogen on the (110) sites has been explained considering that hydrogen would adsorb at the bottom of the rows, leaving the top position available for the oxygen coordination in bridge configuration.

The importance of considering the effect of "spectator" species as key factor to understand the kinetics of ORR has been stressed [147]. This terminology, introduced by N.M. Markovic, refers to adsorbed species (sulfate, OH, and oxides) that interfere with the intermediates of the reaction without participating in it. Their main effect is the decrease of available surface sites for the reaction although they can also exert electronic effects. The coverage of these species depends on several factors such as the structure of the surface and the electrode potential. In this regard, the low activity of Pt(111) in sulfuric acid solutions is not an intrinsic property of this surface but the consequence of the strong adsorption of sulfate anions that forms a rather compact adlayer that blocks the reduction of oxygen. The formation of an ordered structure on this surface even during the course of the ORR is signaled by the observation of the spike corresponding to the order/disorder phase transition [142, 146]. It is puzzling, however, that such adlayer does not favor the two-electron pathway to hydrogen peroxide as the hydrogen adsorption does. The presence of other strongly adsorbed anions such as bromide and chloride does indeed exert a similar effect as hydrogen adsorption does at low potentials, inducing the formation of H_2O_2 [150]. In seems that sulfate adlayer structure is sufficiently open to allow adsorption of O_2-related intermediates on bridge configuration. However, the structure of the adlayer and the strength of the adsorption are important factors in this regard, since the strong adsorption of sulfate on a Pd monolayer on Pt(111) again favors hydrogen peroxide production, even although the structure of the adlayer is expected to be the same [152]. Introduction of steps on the Pt(111) surface disrupts the ordered sulfate structure and decreases the overvoltage necessary for the ORR. When comparing curves in sulfuric acid and perchloric acid solutions, activity is always higher in the latter due to the absence of specific adsorption effects (apart from OH adsorption). The activity of different electrodes for the ORR can be seen as a function of the step density in Figure 1.24. As indicator of activity, values of j_0 can be used, when available. Alternatively, values of $E_{1/2}$ provide also a measure of the relative activity of different surfaces. For both crystallographic zones, the surface with maximum activity is the turning point, that is, the most open surface with equal number of terrace and step atoms. For surfaces with (111) terrace and either (110) or (100) steps, there is always a significant increase in the activity with the introduction of steps. For surfaces with (100) or (110) terraces, the increase in the activity with the

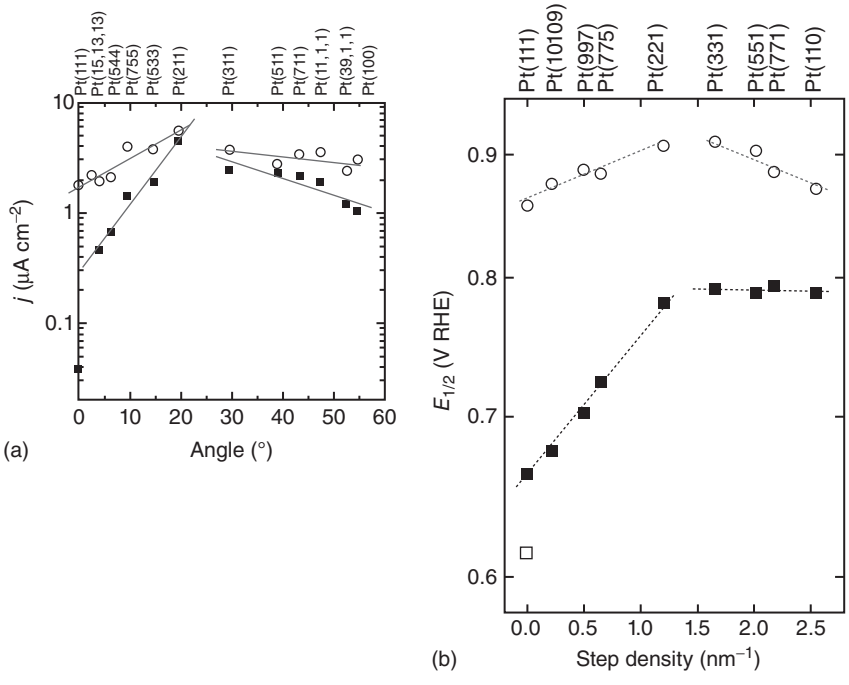

Figure 1.24 Plot of (a) j_0 for the [01$\bar{1}$] zone and (b) $E_{1/2}$ for the [1$\bar{1}$0] zone for ORR as a function of the angle and step density, respectively, in 0.5 M H_2SO_4 (close symbols) and 0.1 M $HClO_4$ (open symbols) (a) Maciá 2004 [146]; b) Kuzume 2007 [142]. Reproduced with permission of Elsevier).

introduction of steps is more moderate, or there is no increase at all, for surfaces with structure $n(110) \times (111)$ in sulfuric acid solutions. One interesting observation is that the extrapolated activity of stepped surfaces with (111) terraces to zero step density does not coincide with the (111) surface. The basal plane exhibits significantly lower activity in comparison with the extrapolated value. This reflects the importance of long-range order on the ordering of the sulfate adlayer. Long-range order is not present on the stepped surfaces, and therefore the extrapolated value reflects the intrinsic activity of the (111) terrace sites in the absence of the long-range order effect.

The effect of "spectator" species is also important for the interpretation of Tafel slopes. For Pt(111) in sulfuric acid solution, a single Tafel slope of 120 mV is obtained in the whole potential range [142, 146, 147]. However in perchloric acid, Tafel slope changes from 60 mV at high potentials, above 0.85 V, to 120 mV at lower potentials. This was interpreted as the result of the change of coverage of spectator species in the potential range of study [147]. According to this interpretation, the correct expression of the Tafel relationship between current and potentials should be

$$j = -4Fkc_b(1 - \theta_A)\exp\left(-\frac{\alpha F}{RT}E\right) \tag{1.61}$$

where k is the kinetic constant, α is the electron transfer coefficient, c_b is the concentration at the solution, and θ_A is the coverage of "spectator" species, either sulfate or OH. It is obvious from this expression that Tafel slope will depend on the value of $(d\theta_A/dE)$.

For sulfuric acid solutions, sulfate coverage is constant in the potential range of kinetic limitation for the ORR, and therefore Tafel slope is not affected by their coverage. However in perchloric acid, OH coverage changes with the potential affecting the value of the Tafel slope. It has been shown that a way to overcome this difficulty is to construct the Tafel plot from current values extrapolated to time zero from a chronoamperometric experiment. In this way, adsorption of oxygenated species is avoided and the expected value of Tafel slope of 120 is obtained. However, if the stationary value of the current after 10 s is used to make the Tafel plot, the slope decreases to 60 mV. For the other electrodes, a similar situation is obtained with the value of Tafel slope of 120 mV prevailing if complications such as those described earlier are avoided.

The important conclusion for this part is that kinetic studies should consider all the constituents of the interphase, since all of them may play a role in determining the rate of the reaction under study. In some cases, sensitivity to the structure of the surface can be an indirect property, which is the consequence of the adsorption of other species interfering with the main reaction.

1.8 Concluding Remarks

The evolution on the last decades of methods for the preparation of electrode surfaces with well-defined crystallographic structures allowed collecting abundant information about the relationship between surface structure and reactivity under precise experimental conditions. It is nowadays possible to prepare complex surfaces composed of different combinations of terraces, steps, and kink sites in a controlled way. The systematic variation of the distribution of different surface geometries and the study of its effect on reactivity allow the separation of the contribution of each surface site to the overall electrochemical behavior. Precise knowledge of the atomic density allows taking coulometric analysis to a level of detail not possible with other polycrystalline materials.

Cyclic voltammetry of platinum under extremely clean conditions is at present rather well understood. This has allowed us getting a relatively detailed picture of the structure of the interphase and its relationship with the nature of the electrode surface and the composition of the solution. Such studies have taught us how sensitive is the electrocatalytic response to surface composition and structure. Minor changes in the composition of the solution result in a significant modification of the cyclic voltammogram. Platinum surfaces are very reactive (therefore their interest as catalytic material), which makes them difficult to study. Organic compounds readily dissociate on platinum to produce residues that accumulate on the surface, changing drastically its reactivity. Also, oxide

formation and subsequent reduction cause disordering of the surface. For these reasons, it is exceedingly important in interfacial studies to carefully control the composition of the solution (cleanliness) and the conditions for decontamination and surface treatment (annealing and cooling atmosphere). This sensitivity to solution contaminations is not limited to well-defined surfaces. Studies involving polycrystalline materials or nanoparticle dispersions are not free from such interferences from solution contaminations, although it is more difficult to identify them. Hence, similar care as that taken with single crystals should also be considered with other polycrystalline electrodes to obtain meaningful results.

In this chapter we have shown the power of the combination of classical electrochemical techniques (cyclic voltammetry, coulometric measurements, capacitance measurements, and double-layer thermodynamics) with the use of well-defined surfaces. Such studies can be complemented with spectroscopic and microscopic measurements to obtain a more detailed picture of the interphase and its effect on electrocatalysis.

The two examples of electrocatalytic studies described earlier, CO oxidation and ORR, have been selected because they explain well how (i) all the knowledge about the structure of the interphase and the parameters that describe it, can be used to obtain a better understanding of the electrocatalytic process and (ii) the systematic introduction of steps on the flat terraces allows to separate the role of different surface sites on the overall reactivity. In regard to the last point, it is important to remark how the extrapolation to zero step density allows the understanding of the reactivity of the ideal terrace in a way that is not achievable through the preparation of the corresponding basal planes, since the real surface will always contain defects that may affect its reactivity in a way that is, in some cases, nonnegligible.

The fact that most electrocatalytic reactions are very sensitive to the surface structure implies that this is a parameter that has to be controlled and understood before the study with complex polycrystalline surfaces can be addressed. The reality is that practical applications cannot be performed with such degree of control. Therefore, the extension from model studies with well-defined surfaces to real catalysts is a challenging issue that requires a significant leap. This can be eased with the help of nanoparticles with preferential shapes. It is nowadays possible to synthesize nanoparticles with a rather homogeneous distribution of crystal shapes exposing surfaces with preferential crystallographic structures [153–157].

Future directions in the field involve the study of nonaqueous electrolytes and bimetallic or multimetallic materials. In this regard, a lot of attention is given at present to ionic liquids and to the characterization of the electrochemical interphase in contact with them and its effect on reactivity [158–160]. Regarding bimetallic electrodes, it is clear that best electrocatalysts involve the combination of more than one metal in order to tailor the electronic properties of the material to the reaction under scope. However, there is still a lot to be learned about the interfacial properties of these materials.

Acknowledgments

Support from MINECO (Spain) through projects CTQ2013-44083-P and CTQ2016-76221-P and Generalitat Valenciana through project PROMETEOII/2014/013 is greatly acknowledged.

References

1. Herrero, E., Feliu, J.M., and Aldaz, A. (2003) in *Encyclopedia of Electrochemistry*, vol. **2** (eds A.J. Bard and M. Stratmann), Wiley-VCH Verlag GmbH, Weinheim, p. 443.
2. Clavilier, J., Faure, R., Guinet, G., and Durand, R. (1980) Preparation of monocrystalline Pt microelectrodes and electrochemical study of the plane surfaces cut in the direction of the {111} and {110} planes. *J. Electroanal. Chem.*, **107**, 205–209.
3. Clavilier, J. (1980) The role of anion on the electrochemical behaviour of a {111} platinum surface; an unusual splitting of the voltammogram in the hydrogen region. *J. Electroanal. Chem.*, **107**, 211–216.
4. Will, F.G. (1965) Hydrogen adsorption on platinum single crystal electrodes. I. Isotherms and heats of adsorption. *J. Electrochem. Soc.*, **112**, 451–455.
5. O'Grady, W.E., Woo, M.Y.C., Hagans, P.L., and Yeager, E. (1977) Electrode surface studies by Leed-Auger. *J. Vac. Sci. Technol.*, **14**, 365–368.
6. Hubbard, A.T., Ishikawa, R.M., and Katekaru, J. (1978) Study of platinum electrodes by means of electrochemistry and low energy electron diffraction. 2. Comparison of electrochemical activity of Pt(100) and Pt(111) surfaces. *J. Electroanal. Chem.*, **86**, 271–288.
7. Yeager, E., O'Grady, W.E., Woo, M.Y.C., and Hagen, P. (1978) Hydrogen adsorption on single crystal platinum. *J. Electrochem. Soc.*, **125**, 348–349.
8. Ross, P.N. (1979) Structure sensitivity in the electrocatalytic properties of platinum. I. Hydrogen adsorption on low index single crystal and the role of steps. *J. Electrochem. Soc.*, **126**, 67–77.
9. Clavilier, J., Rodes, A., El Achi, K., and Zamakhchari, M.A. (1991) Electrochemistry at platinum single crystal surfaces in acidic media: hydrogen and oxygen adsorption. *J. Chim. Phys.*, **88**, 1291–1337.
10. Wagner, F.T. and Ross, P.N. (1988) Long-range structural effects in the anomalous voltammetry on ultra-high vacuum prepared Pt (111). *J. Electroanal. Chem.*, **250**, 301–320.
11. Climent, V. and Feliu, J.M. (2011) Thirty years of platinum single crystal electrochemistry. *J. Solid State Electrochem.*, **15**, 1297–1315.
12. Korzeniewski, C., Climent, V., and Feliu, J. (2011) in *Electroanalytical Chemistry: A Series of Advances*, vol. **24** (eds A.J. Bard and C.G. Zoski), CRC Press, Boca Raton, FL, pp. 75–170.
13. Masel, R.I. (1996) *Principles of Adsorption and Reaction on Solid Surfaces*, John Wiley & Sons, Inc., New York.
14. Somorjai, G. and Li, Y. (2010) *Introduction to Surface Chemistry and Catalysis*, 2nd edn, Willey.
15. Barrett, C.S. and Massalski, T.B. (1980) *Structure of Metals: Crystallographic Methods, Principles and Data*, 3rd edn, Pergamon, Oxford, New York, p. xv, 654 pp.
16. Hamelin, A. (1985) *Modern Aspects of Electrochemistry*, vol. **16** (eds B.E. Conway, R.E. White and J.O.M. Bockris), Plenum, New York, pp. 1–101.
17. Lide, D.R. and Frederikse, H.P.R. (1998) *CRC Handbook of Chemistry and Physics*, vol. **79**, CRC Press, Boca Raton, FL.
18. Lang, B., Joyner, R.W., and Somorjai, G.A. (1972) LEED studies of high index crystal surfaces of platinum. *Surf. Sci.*, **30**, 440.

19. Feliu, J.M., Herrero, E., and Climent, V. (2011) in *Catalysis in Electrochemistry* (eds E. Santos and W. Schmickler), John Wiley & Sons, Inc., Hoboken, NJ, pp. 127–163.
20. Chen, Q. and Richardson, N.V. (2004) Physical studies of chiral surfaces. *Annu. Rep. Prog. Chem. Sect. C: Phys. Chem.*, **100**, 313–347.
21. Sholl, D.S., Asthagiri, A., and Power, T.D. (2001) Naturally chiral metal surfaces as enantiospecific adsorbents. *J. Phys. Chem. B*, **105**, 4771–4782.
22. Ahmadi, A., Attard, G., Feliu, J., and Rodes, A. (1999) Surface reactivity at "chiral" platinum surfaces. *Langmuir*, **15**, 2420–2424.
23. Attard, G.A., Clavilier, J., and Feliu, J.M. (2002) Chirality at well-defined metal surfaces. *ACS Symp. Ser.*, **810**, 254–268.
24. Cuesta, A., Kibler, L.A., and Kolb, D.M. (1999) A method to prepare single crystal electrodes of reactive metals: application to Pd(hkl). *J. Electroanal. Chem.*, **466**, 165–168.
25. Clavilier, J. (1999) in *Interfacial Electrochemistry* (ed. A. Wieckowski), Marcel Dekker, Inc., New York, pp. 231–248.
26. Dickertmann, D., Koppitz, F.D., and Schultze, J.W. (1976) A method for elimination of side effects on electrochemical measurements of single crystals. Additional test of the adsorption systems silver-lead ion and gold-cupric ion. *Electrochim. Acta*, **21**, 967–971.
27. Aberdam, D., Durand, R., Faure, R., and El-Omar, F. (1986) Structural changes of a Pt(111) electrode induced by electrosorption of oxygen in acidic solutions: a coupled voltammetry, LEED and AES study. *Surf. Sci.*, **171**, 303–330.
28. Clavilier, J., El Achi, K., Petit, M., Rodes, A., and Zamakhchari, M.A. (1990) Electrochemical monitoring of the thermal reordering of platinum single crystal surfaces after metallographic polishing from the early stage to the equilibrium surfaces. *J. Electroanal. Chem.*, **295**, 333.
29. Clavilier, J., Armand, D., and Wu, B.L. (1982) Electrochemical study of the initial surface condition of platinum surfaces with (100) and (111) orientations. *J. Electroanal. Chem.*, **135**, 159–166.
30. Clavilier, J., Feliu, J.M., Fernández-Vega, A., and Aldaz, A. (1989) Electrochemical behavior of irreversibly adsorbed bismuth on Pt(100) with different degrees of crystalline surface order. *J. Electroanal. Chem.*, **269**, 175–189.
31. Itaya, K., Sugawara, S., Sashikata, K., and Furuya, N. (1990) In situ scanning tunneling microscopy of platinum (111) surface with the observation of monatomic steps. *J. Vac. Sci. Technol., A*, **8**, 515–519.
32. Climent, V. and Feliu, J.M. (2015) Cyclic voltammetry, in *Reference Module in Chemistry, Molecular Sciences and Chemical Engineering* (ed. J. Reedijk), Elsevier, Amsterdam.
33. Jaaf-Golze, K.A., Kolb, D.M., and Scherson, D. (1986) On the voltammetry of curves of Pt (111) in aqueous solutions. *J. Electroanal. Chem.*, **200**, 353–362.
34. Clavilier, J., Albalat, R., Gómez, R., Orts, J.M., Feliu, J.M., and Aldaz, A. (1992) Study of the charge displacement at constant potential during CO adsorption on Pt(110) and Pt(111) electrodes in contact with a perchloric acid solution. *J. Electroanal. Chem.*, **330**, 489–497.
35. Clavilier, J., Albalat, R., Gómez, R., Orts, J.M., and Feliu, J.M. (1993) Displacement of adsorbed iodine on platinum single-crystal electrodes by irreversible adsorption of CO at controlled potential. *J. Electroanal. Chem.*, **360**, 325–335.
36. Orts, J.M., Gómez, R., Feliu, J.M., Aldaz, A., and Clavilier, J. (1994) Potentiostatic charge displacement by exchanging adsorbed species on Pt(111) electrodes—acidic electrolytes with specific anion adsorption. *Electrochim. Acta*, **39**, 1519–1524.
37. Feliu, J.M., Orts, J.M., Gómez, R., Aldaz, A., and Clavilier, J. (1994) New information on the unusual adsorption states of Pt(111) in sulphuric acid solutions from potentiostatic adsorbate

replacement by CO. *J. Electroanal. Chem.*, **372**, 265–268.
38. Clavilier, J., Orts, J.M., Gómez, R., Feliu, J.M., and Aldaz, A. (1994) in *The Electrochemical Society Proceedings*, vol. **94-21** (eds B.E. Conway and G. Jerkiewicz), The Electrochemical Society, Inc., Pennington, NJ, pp. 167–183.
39. Climent, V., Gómez, R., and Feliu, J.M. (1999) Effect of increasing amount of steps on the potential of zero total charge of Pt(111) electrodes. *Electrochim. Acta*, **45**, 629–637.
40. Gómez, R., Climent, V., Feliu, J.M., and Weaver, M.J. (2000) Dependence of the potential of zero charge of stepped platinum (111) electrodes on the oriented step-edge density: electrochemical implications and comparison with work function behavior. *J. Phys. Chem. B*, **104**, 597–605.
41. Herrero, E., Feliu, J.M., Wieckowski, A., and Clavilier, J. (1995) The unusual adsorption states of Pt(111) electrodes studied by an iodine displacement method: comparison with Au(111) electrodes. *Surf. Sci.*, **325**, 131–138.
42. Funtikov, A.M., Stimming, U., and Vogel, R. (1997) Anion adsorption from sulfuric acid solutions on Pt(111) single crystal electrodes. *J. Electroanal. Chem.*, **428**, 147–153.
43. Braunschweig, B. and Daum, W. (2009) Superstructures and order/disorder transition of sulfate adlayers on Pt(111) in sulfuric acid solution. *Langmuir*, **25**, 11112–11120.
44. Faguy, P.W., Markovic, N., Adzic, R.R., Fierro, C.A., and Yeager, E. (1990) A study of bisulfate adsorption on Pt(111) single crystal electrodes using in-situ Fourier transform infrared spectroscopy. *J. Electroanal. Chem.*, **289**, 245.
45. Ogasawara, H., Sawatari, Y., Inukai, J., and Ito, M. (1993) Adsorption of bisulfate anion on a Pt(111) electrode: a comparison of in-situ and ex-situ IRAS. *J. Electroanal. Chem.*, **358**, 337.
46. Sawatari, Y., Inukai, J., and Ito, M. (1993) The structure of bisulfate and perchlorate on a Pt(111) electrode surface studied by infrared spectroscopy and ab-initio molecular orbital calculation. *J. Electron. Spectrosc. Relat. Phenom.*, **64–65**, 515.
47. Nart, F.C., Iwasita, T., and Weber, M. (1994) Vibrational spectroscopy of adsorbed sulfate on Pt(111). *Electrochim. Acta*, **39**, 961.
48. Faguy, P.W., Marinkovic, N.S., and Adzic, R.R. (1996) An in-situ infrared study on the effect of pH on anion adsorption at Pt(111) electrodes from acid sulfate-solutions. *Langmuir*, **12**, 243–247.
49. Faguy, P.W., Marinkovic, N.S., and Adzic, R.R. (1996) Infrared spectroscopic analysis of anions adsorbed from bisulfate-containing solutions on Pt(111) electrodes. *J. Electroanal. Chem.*, **407**, 209–218.
50. Shingaya, Y., Hirota, K., Ogasawara, H., and Ito, M. (1996) Infrared spectroscopic study of electric double layers on Pt(111) under electrode reactions in a sulfuric acid solution. *J. Electroanal. Chem.*, **409**, 103–108.
51. Shingaya, Y. and Ito, M. (1996) Interconversion of a bisulfate anion into a sulfuric acid molecule on a Pt(111) electrode in a 0.5 M H2SO4 solution. *Chem. Phys. Lett.*, **256**, 438–444.
52. Shingaya, Y. and Ito, M. (1996) Coordination number and molecular orientation of hydronium cation bisulfate anion adlayers on Pt(111). *Surf. Sci.*, **368**, 318–323.
53. Lachenwitzer, A., Li, N., and Lipkowski, J. (2002) Determination of the acid dissociation constant for bisulfate adsorbed at the Pt(111) electrode by subtractively normalized interfacial Fourier transform infrared spectroscopy. *J. Electroanal. Chem.*, **532**, 85–98.
54. Su, Z.F., Climent, V., Leitch, J., Zamlynny, V., Feliu, J.M., and Lipkowski, J. (2010) Quantitative SNIFTIRS studies of (bi)sulfate adsorption at the Pt(111) electrode surface. *Phys. Chem. Chem. Phys.*, **12**, 15231–15239.
55. Kolics, A. and Wieckowski, A. (2001) Adsorption of bisulfate and sulfate anions on a Pt(111) electrode. *J. Phys. Chem. B*, **105**, 2588–2595.

56. Fromondi, I. and Scherson, D. (2007) (Bi)Sulfate adsorption on quasiperfect Pt(111) facets from acidic aqueous electrolytes as monitored by optical techniques. *J. Phys. Chem. C*, **111**, 10154–10157.

57. Berna, A., Feliu, J.M., Gancs, L., and Mukerjee, S. (2008) Voltammetric characterization of Pt single crystal electrodes with basal orientations in trifluoromethanesulphonic acid. *Electrochem. Commun.*, **10**, 1695–1698.

58. Rudnev, A.V. and Wandlowski, T. (2012) An influence of pretreatment conditions on surface structure and reactivity of Pt(100) towards CO oxidation reaction. *Russ. J. Electrochem.*, **48**, 259–270.

59. Clavilier, J., Orts, J.M., and Feliu, J.M. (1994) Etude de l'effet de prétraitements sur la topographie des surfaces orientées de platine par deux méthodes indépendates: voltammétrie et STM. *J. Phys. IV*, **4**, 1–303.

60. Attard, G.A., Hazzazi, O., Wells, P.B., Climent, V., Herrero, E., and Feliu, J.M. (2004) On the global and local values of the potential of zero total charge at well-defined platinum surfaces: stepped and adatom modified surfaces. *J. Electroanal. Chem.*, **568**, 329–342.

61. Climent, V., Gómez, R., Orts, J.M., and Feliu, J.M. (2006) Thermodynamic analysis of the temperature dependence of OH adsorption on Pt(111) and Pt(100) electrodes in acidic media in the absence of specific anion adsorption. *J. Phys. Chem. B*, **110**, 11344–11351.

62. AlAkl, A., Attard, G.A., Price, R., and Timothy, B. (1999) Voltammetric and UHV characterization of the (1x1) and reconstructed hex-R0.7 phases of Pt(100). *J. Electroanal. Chem.*, **467**, 60–66.

63. Feliu, J.M., Rodes, A., Orts, J.M., and Clavilier, J. (1994) The problem of surface order of pt single-crystals in electrochemistry. *Pol. J. Chem.*, **68**, 1575–1595.

64. Kibler, L.A., Cuesta, A., Kleinert, M., and Kolb, D.M. (2000) In-situ STM characterisation of the surface morphology of platinum single crystal electrodes as a function of their preparation. *J. Electroanal. Chem.*, **484**, 73–82.

65. Souza-Garcia, J., Climent, V., and Feliu, J.M. (2009) Voltammetric characterization of stepped platinum single crystal surfaces vicinal to the (110) pole. *Electrochem. Commun.*, **11**, 1515–1518.

66. Attard, G.A. and Brew, A. (2015) Cyclic voltammetry and oxygen reduction activity of the Pt{110}-(1 x 1) surface. *J. Electroanal. Chem.*, **747**, 123–129.

67. Hurwitz, H.D. (1965) Direct determination of the surface excess of specifically adsorbed ions on mercury. *J. Electroanal. Chem.*, **10**, 35–41.

68. Dutkiewicz, E. and Parsons, R. (1966) The adsorption of iodide ion from aqueous KI + KF of constant ionic strength. *J. Electroanal. Chem.*, **11**, 100–110.

69. Mohilner, D.M. (1966) in *The Electrical Double Layer. Part I. Elements of Double-Layer Theory*, vol. **1** (ed. A.J. Bard), Marcel Dekker, Inc., New York, pp. 241–409.

70. Bockris, J.O.M., Argade, S.D., and Gileadi, E. (1969) The determination of the potential of zero charge on solid metals. *Electrochim. Acta*, **14**, 1259–1283.

71. Hamelin, A. and Stoicoviciu, L. (1987) Study of gold low index faces in KPF_6 solutions. 1. Experimental behavior and determination of the points of zero charge. *J. Electroanal. Chem.*, **234**, 93–105.

72. Bachetta, M., Trasatti, S., Doubova, L., and Hamelin, A. (1986) The dependence of the potential of zero charge of silver electrodes on the crystallographic orientation of the surface. *J. Electroanal. Chem.*, **200**, 389–396.

73. Lecoeur, J., Andro, J., and Parsons, R. (1982) The behaviour of water at stepped surfaces of single crystal gold electrodes. *Surf. Sci.*, **114**, 320–330.

74. Parsons, R. (1980) *Comprehensive Treatise of Electrochemistry*, vol. **1** (eds J.O.M. Bockris, B.E. Conway and E. Yeager), Plenum, New York, pp. 1–44.

75. Frumkin, A.N. and Petrii, O.A. (1975) Potentials of zero total charge and zero

free charge of platinum group metals. *Electrochim. Acta*, **20**, 347–359.
76. Frumkin, A.N., Petrii, O.A., and Damaskin, B.B. (1980) *Comprehensive Treatise of Electrochemistry*, vol. **1**, Plenum, New York, pp. 221–289.
77. Garcia-Araez, N., Climent, V., Herrero, E., Feliu, J.M., and Lipkowski, J. (2006) Thermodynamic approach to the double layer capacity of a Pt(111) electrode in perchloric acid solutions. *Electrochim. Acta*, **51**, 3787–3793.
78. Rizo, R., Sitta, E., Herrero, E., Climent, V., and Feliu, J.M. (2015) Towards the understanding of the interfacial pH scale at Pt(111) electrodes. *Electrochim. Acta*, **162**, 138–145.
79. Climent, V., Gómez, R., Orts, J.M., Aldaz, A., and Feliu, J.M. (1997) *The Electrochemical Society Proceedings (Electrochemical Double Layer)*, vol. **97-17** (eds C. Korzeniewski and B.E. Conway), The Electrochemical Society, Inc., Pennington, NJ, pp. 222–237.
80. Climent, V., Gómez, R., Orts, J.M., Aldaz, A., and Feliu, J.M. (2000) *Potential of Zero Total Charge of Platinum Single Crystal Electrodes*, vol. **2000-16** (eds G. Jerkiewicz, J.M. Feliu and B.N. Popov), The Electrochemical Society, Inc., Pennington, NJ, pp. 12–30.
81. Weaver, M.J. (1998) Potentials of zero charge for platinum(111)-aqueous interfaces: a combined assessment from in-situ and ultrahigh-vacuum measurements. *Langmuir*, **14**, 3932–3936.
82. Cuesta, A. (2004) Measurement of the surface charge density of CO-saturated Pt(111) electrodes as a function of potential: the potential of zero charge of Pt(111). *Surf. Sci.*, **572**, 11–22.
83. Villegas, I. and Weaver, M.J. (1994) Carbon-monoxide adlayer structures on platinum(111) electrodes – a synergy between in-situ scanning-tunneling-microscopy and infrared-spectroscopy. *J. Chem. Phys.*, **101**, 1648–1660.
84. Markovic, N.M., Lucas, C.A., Rodes, A., Stamenkovic, V., and Ross, P.N. (2002) Surface electrochemistry of CO on Pt(111): anion effects. *Surf. Sci.*, **499**, L149–L158.
85. Rodes, A., Gómez, R., Feliu, J.M., and Weaver, M.J. (2000) Sensitivity of compressed carbon monoxide adlayers on platinum(III) electrodes to long-range substrate structure: influence-of monoatomic steps. *Langmuir*, **16**, 811–816.
86. Gómez, R., Feliu, J.M., Aldaz, A., and Weaver, M.J. (1998) Validity of double-layer charge-corrected voltammetry for assaying carbon monoxide coverages on ordered transition metals: comparisons with adlayer structures in electrochemical and ultrahigh vacuum environments. *Surf. Sci.*, **410**, 48–61.
87. Climent, V., Garcia-Araez, N., Herrero, E., and Feliu, J. (2006) Potential of zero total charge of platinum single crystals: a local approach to stepped surfaces vicinal to Pt(111). *Russ. J. Electrochem.*, **42**, 1145–1160.
88. Garcia-Araez, N., Climent, V., Herrero, E., Feliu, J., and Lipkowski, J. (2005) Thermodynamic studies of chloride adsorption at the Pt(111) electrode surface from 0.1 M $HClO_4$ solution. *J. Electroanal. Chem.*, **576**, 33–41.
89. Garcia-Araez, N., Climent, V., Herrero, E., Feliu, J., and Lipkowski, J. (2006) Thermodynamic studies of bromide adsorption at the Pt(111) electrode surface perchloric acid solutions: comparison with other anions. *J. Electroanal. Chem.*, **591**, 149–158.
90. Rodes, A., Climent, V., Orts, J.M., Pérez, J.M., and Aldaz, A. (1998) Nitric oxide adsorption at Pt(100) electrode surfaces. *Electrochim. Acta*, **44**, 1077–1090.
91. Rodes, A., Gómez, R., Perez, J.M., Feliu, J.M., and Aldaz, A. (1996) On the voltammetric and spectroscopic characterization of nitric oxide adlayers formed from nitrous acid on Pt(h,k,1) and Rh(h,k,1) electrodes. *Electrochim. Acta*, **41**, 729–745.
92. Martinez-Hincapie, R., Sebastian-Pascual, P., Climent, V., and Feliu, J.M. (2015) Exploring the interfacial neutral pH region of Pt(111) electrodes. *Electrochem. Commun.*, **58**, 62–64.
93. Shi, Z. and Lipkowski, J. (1994) Investigations of SO_4^{2-} adsorption at the

Au(111) electrode in the presence of underpotentially deposited copper adatoms. *J. Electroanal. Chem.*, **364**, 289–294.

94. Shi, Z., Lipkowski, J., Gamboa, M., Zelenay, P., and Wieckowski, A. (1994) Investigations of SO_4^{2-} adsorption at the Au(111) electrode by chronocoulometry and radiochemistry. *J. Electroanal. Chem.*, **366**, 317–326.
95. Shi, Z.C. and Lipkowski, J. (1996) Chloride adsorption at the Au(111) electrode surface. *J. Electroanal. Chem.*, **403**, 225–239.
96. Lipkowski, J., Shi, Z.C., Chen, A.C., Pettinger, B., and Bilger, C. (1998) Ionic adsorption at the Au(111) electrode. *Electrochim. Acta*, **43**, 2875–2888.
97. Lipkowski, J., Schmickler, W., Kolb, D.M., and Parsons, R. (1998) Comments on the thermodynamics of solid electrodes. *J. Electroanal. Chem.*, **452**, 193–197.
98. Herrero, E., Mostany, J., Feliu, J.M., and Lipkowski, J. (2002) Thermodynamic studies of anion adsorption at the Pt(111) electrode surface in sulfuric acid solutions. *J. Electroanal. Chem.*, **534**, 79–89.
99. Mostany, J., Herrero, E., Feliu, J.M., and Lipkowski, J. (2002) Thermodynamic studies of anion adsorption at stepped platinum(hkl) electrode surfaces in sulfuric acid solutions. *J. Phys. Chem. B*, **106**, 12787–12796.
100. Mostany, J., Herrero, E., Feliu, J.M., and Lipkowski, J. (2003) Determination of the Gibbs excess of H and OH adsorbed at a Pt(111) electrode surface using a thermodynamic method. *J. Electroanal. Chem.*, **558**, 19–24.
101. Garcia-Araez, N., Climent, V., Herrero, E., Feliu, J.M., and Lipkowski, J. (2005) Determination of the Gibbs excess of H adsorbed at a Pt(111) electrode surface in the presence of co-adsorbed chloride. *J. Electroanal. Chem.*, **582**, 76–84.
102. Garcia-Araez, N., Climent, V., Rodríguez, P., and Feliu, J.M. (2008) Thermodynamic analysis of (bi)sulphate adsorption on a Pt(111) electrode as a function of pH. *Electrochim. Acta*, **53**, 6793–6806.
103. Mostany, J., Martinez, P., Climent, V., Herrero, E., and Feliu, J.M. (2009) Thermodynamic studies of phosphate adsorption on Pt(111) electrode surfaces in perchloric acid solutions. *Electrochim. Acta*, **54**, 5836–5843.
104. Garcia-Araez, N., Climent, V., Rodriguez, P., and Feliu, J.M. (2010) Thermodynamic evidence for K^+-SO_4^{2-} ion pair formation on Pt(111). New insight into cation specific adsorption. *Phys. Chem. Chem. Phys.*, **12**, 12146–12152.
105. Benderskii, V.A. and Velichko, G.I. (1982) Temperature jump in electric double-layer study. Part I. Method of measurements. *J. Electroanal. Chem.*, **140**, 1–22.
106. Smalley, J.F., Krishnan, C.V., Goldman, M., Feldberg, S.W., and Ruzic, I. (1988) Laser-induced temperature-jump coulostatics for the investigation of heterogeneous rate processes. Theory and application. *J. Electroanal. Chem.*, **248**, 255–282.
107. Climent, V., Coles, B.A., and Compton, R.G. (2002) Coulostatic potential transients induced by laser heating of a Pt(111) single-crystal electrode in aqueous acid solutions. Rate of hydrogen adsorption and potential of maximum entropy. *J. Phys. Chem. B*, **106**, 5988–5996.
108. Climent, V., Coles, B.A., and Compton, R.G. (2002) Laser-induced potential transients on a Au(111) single-crystal electrode. Determination of the potential of maximum entropy of double layer formation. *J. Phys. Chem. B*, **106**, 5258–5265.
109. Climent, V., Coles, B.A., Compton, R.G., and Feliu, J.M. (2004) Coulostatic potential transients induced by laser heating of platinum stepped electrodes: influence of steps on the entropy of double layer formation. *J. Electroanal. Chem.*, **561**, 157–165.
110. Climent, V., Garcia-Araez, N., Compton, R.G., and Feliu, J.M. (2006) Effect of deposited bismuth on the potential of maximum entropy of Pt(111) single-crystal electrodes. *J. Phys. Chem. B*, **110**, 21092–21100.

111. Garcia-Araez, N., Climent, V., and Feliu, J.M. (2008) Evidence of water reorientation on model electrocatalytic surfaces from nanosecond-laser-pulsed experiments. *J. Am. Chem. Soc.*, **130**, 3824–3833.
112. Garcia-Araez, N., Climent, V., and Feliu, J. (2009) Potential-dependent water orientation on Pt(111), Pt(100), and Pt(110), as inferred from laser-pulsed experiments. Electrostatic and chemical effects. *J. Phys. Chem. C*, **113**, 9290–9304.
113. Garcia-Araez, N., Climent, V., and Feliu, J.M. (2009) Potential-dependent water orientation on Pt(111) stepped surfaces from laser-pulsed experiments. *Electrochim. Acta*, **54**, 966–977.
114. Agar, J.N. (1963) *Thermogalvanic Cells*, vol. **3** (eds P. Delahay and C.W. Tobias), Wiley-Interscience, New York, pp. 31–121.
115. Garcia-Araez, N., Climent, V., and Feliu, J.M. (2011) in *Modern Aspects of Electrochemistry*, vol. **51** (ed. C.G. Vayenas), Springer, pp. 1–105.
116. Chang, S.C. and Weaver, M.J. (1990) Coverage and potential-dependent binding geometries of carbon monoxide at ordered low-index platinum and rhodium-aqueous interfaces: comparisons with adsorption in corresponding metal-vacuum environments. *Surf. Sci.*, **238**, 142.
117. Chang, S.C. and Weaver, M.J. (1990) In situ infrared spectroscopy of CO adsorbed at ordered Pt(100)-aqueous interfaces: double layer effects upon the adsorbate binding geometry. *J. Phys. Chem.*, **94**, 5095.
118. Chang, S.C. and Weaver, M.J. (1990) Coverage dependent dipole coupling for carbon monoxide adsorbed at ordered Pt(111)-aqueous interfaces: structural and electrochemical implications. *J. Chem. Phys.*, **92**, 4582.
119. Chang, S.C., Jiang, X., Roth, J.D., and Weaver, M.J. (1991) Influence of potential on metal-adsorbate structure: solvent independent nature of infrared spectra for Pt(111)/CO. *J. Phys. Chem.*, **95**, 5378.
120. Vitus, C.M., Chang, S.C., Schardt, B.C., and Weaver, M.J. (1991) In situ scanning tunneling microscopy as a probe of adsorbate-induced reconstruction at ordered monocrystalline electrodes: CO on Pt(100). *J. Phys. Chem.*, **95**, 7559–7563.
121. Jiang, X. and Weaver, M.J. (1992) The role of interfacial potential in adsorbate bonding: electrode potential dependent infrared spectra of saturated CO adlayers on Pt(110) and related electrochemical surfaces in varying solvent environments. *Surf. Sci.*, **275**, 237.
122. Kizhakevariam, N., Villegas, I., and Weaver, M.J. (1995) Model electrochemical interfaces in ultrahigh-vacuum – solvent effects upon coverage-dependent infrared-spectra of carbon-monoxide on platinum(111). *Langmuir*, **11**, 2777–2786.
123. Severson, M.W., Stuhlmann, C., Villegas, I., and Weaver, M.J. (1995) Dipole-dipole coupling effects upon infrared-spectroscopy of compressed electrochemical adlayers – application to the Pt(111)/CO system. *J. Chem. Phys.*, **103**, 9832–9843.
124. Lucas, C.A., Markovic, N.M., and Ross, P.N. (1999) The adsorption and oxidation of carbon monoxide at the Pt(111)/electrolyte interface: atomic structure and surface relaxation. *Surf. Sci.*, **425**, L381–L386.
125. Tolmachev, Y.V., Menzel, A., Tkachuk, A.V., Chu, Y.S., and You, H.D. (2004) In situ surface X-ray scattering observation of long-range ordered (root 19 x root 19)R23.4 degrees-13CO structure on Pt(111) in aqueous electrolytes. *Electrochem. Solid-State Lett.*, **7**, E23–E26.
126. Wang, J.X., Robinson, I.K., Ocko, B.M., and Adzic, R.R. (2005) Adsorbate-geometry specific subsurface relaxation in the CO/Pt(111) system. *J. Phys. Chem. B*, **109**, 24–26.
127. Lucas, C.A. *et al.* (2009) Temperature-induced ordering of metal/adsorbate structures at electrochemical interfaces. *J. Am. Chem. Soc.*, **131**, 7654–7661.
128. Parsons, R. and Vandernoot, T. (1988) The oxidation of small organic-molecules – a survey of recent fuel-cell

related research. *J. Electroanal. Chem.*, **257**, 9–45.

129. Lebedeva, N.P., Koper, M.T.M., Feliu, J.M., and van Santen, R.A. (2002) Role of crystalline defects in electrocatalysis: mechanism and kinetics of CO adlayer oxidation on stepped platinum electrodes. *J. Phys. Chem. B*, **106**, 12938–12947.
130. Lebedeva, N.P., Koper, M.T.M., Feliu, J.M., and van Santen, R.A. (2002) Mechanism and kinetics of the electrochemical CO adlayer oxidation on Pt(111). *J. Electroanal. Chem.*, **524**, 242–251.
131. Lai, S.C.S., Lebedeva, N.P., Housmans, T.H.M., and Koper, M.T.M. (2007) Mechanisms of carbon monoxide and methanol oxidation at single-crystal electrodes. *Top. Catal.*, **46**, 320–333.
132. Petukhov, A.V. (1997) Effect of molecular mobility on kinetics of an electrochemical Langmuir-Hinshelwood reaction. *Chem. Phys. Lett.*, **277**, 539–544.
133. Petukhov, A.V., Akemann, W., Friedrich, K.A., and Stimming, U. (1998) Kinetics of electrooxidation of a CO monolayer at the platinum/electrolyte interface. *Surf. Sci.*, **402**, 182–186.
134. Schmickler, W. and Santos, E. (2010) *Interfacial Electrochemistry*, 2nd edn, Springer, Heidelberg, New York, p. xiv, 272 pp.
135. Lebedeva, N.P., Rodes, A., Feliu, J.M., Koper, M.T.M., and van Santen, R.A. (2002) Role of crystalline defects in electrocatalysis: CO adsorption and oxidation on stepped platinum electrodes as studied by in situ infrared spectroscopy. *J. Phys. Chem. B*, **106**, 9863–9872.
136. Herrero, E., Climent, V., and Feliu, J.M. (2000) On the different adsorption behavior of bismuth, sulfur, selenium and tellurium on a Pt(775) stepped surface. *Electrochem. Commun.*, **2**, 636–640.
137. Markovic, N.M., Grgur, B.N., Lucas, C.A., and Ross, P.N. (1999) Electrooxidation of CO and H_2/CO mixtures on Pt(111) in acid solutions. *J. Phys. Chem. B*, **103**, 487–495.
138. López-Cudero, A., Cuesta, A., and Gutiérrez, C. (2005) Potential dependence of the saturation CO coverage of Pt electrodes: the origin of the prepeak in CO-stripping voltammograms. Part 1: Pt(1 1 1). *J. Electroanal. Chem.*, **579**, 1–12.
139. Farias, M.J.S., Tanaka, A.A., Tremiliosi, G., and Feliu, J.M. (2011) On the apparent lack of preferential site occupancy and electrooxidation of CO adsorbed at low coverage onto stepped platinum surfaces. *Electrochem. Commun.*, **13**, 338–341.
140. Lebedeva, N.P., Koper, M.T.M., Herrero, E., Feliu, J.M., and van Santen, R.A. (2000) CO oxidation on stepped Pt n(111) x (111) electrodes. *J. Electroanal. Chem.*, **487**, 37–44.
141. Farias, M.J.S., Herrero, E., and Feliu, J.M. (2013) Site selectivity for CO adsorption and stripping on stepped and kinked platinum surfaces in alkaline medium. *J. Phys. Chem. C*, **117**, 2903–2913.
142. Kuzume, A., Herrero, E., and Feliu, J.M. (2007) Oxygen reduction on stepped platinum surfaces in acidic media. *J. Electroanal. Chem.*, **599**, 333–343.
143. Markovic, N.M., Gasteiger, H.A., and Ross, P.N. (1995) Oxygen reduction on platinum low-index single-crystal surfaces in sulfuric-acid-solution – rotating ring-Pt(Hkl) disk studies. *J. Phys. Chem.*, **99**, 3411–3415.
144. Markovic, N.M., Gasteiger, H.A., and Philip, N. (1996) Oxygen reduction on platinum low-index single-crystal surfaces in alkaline solution: rotating ring disk(Pt(hkl)) studies. *J. Phys. Chem. B*, **100**, 6715–6721.
145. Grgur, B.N., Markovic, N.M., and Ross, P.N. (1997) Temperature-dependent oxygen electrochemistry on platinum low-index single-crystal surfaces in acid-solutions. *Can. J. Chem.*, **75**, 1465–1471.
146. Maciá, M.D., Campina, J.M., Herrero, E., and Feliu, J.M. (2004) On the kinetics of oxygen reduction on platinum stepped surfaces in acidic media. *J. Electroanal. Chem.*, **564**, 141–150.
147. Wang, J.X., Markovic, N.M., and Adzic, R.R. (2004) Kinetic analysis of oxygen

reduction on Pt(111) in acid solutions: intrinsic kinetic parameters and anion adsorption effects. *J. Phys. Chem. B*, **108**, 4127–4133.

148. Gomez-Marin, A.M. and Feliu, J.M. (2013) New insights into the oxygen reduction reaction mechanism on Pt(111): a detailed electrochemical study. *ChemSusChem*, **6**, 1091–1100.
149. Gomez-Marin, A.M., Rizo, R., and Feliu, J.M. (2014) Oxygen reduction reaction at Pt single crystals: a critical overview. *Catal. Sci. Technol.*, **4**, 1685–1698.
150. Markovic, N.M., Gasteiger, H.A., Grgur, B.N., and Ross, P.N. (1999) Oxygen reduction reaction on Pt(111): effects of bromide. *J. Electroanal. Chem.*, **467**, 157–163.
151. Mayrhofer, K.J.J., Strmcnik, D., Blizanac, B.B., Stamenkovic, V., Arenz, M., and Markovic, N.M. (2008) Measurement of oxygen reduction activities via the rotating disc electrode method: from Pt model surfaces to carbon-supported high surface area catalysts. *Electrochim. Acta*, **53**, 3181–3188.
152. Climent, V., Markovic, N.M., and Ross, P.N. (2000) Kinetics of oxygen reduction on an epitaxial film of palladium on Pt(111). *J. Phys. Chem. B*, **104**, 3116–3120.
153. Vidal-Iglesias, F.J., Solla-Gullón, J., Rodríguez, P., Herrero, E., Montiel, V., Feliu, J.M., and Aldaz, A. (2004) Shape-dependent electrocatalysis: ammonia oxidation on platinum nanoparticles with preferential (100) surfaces. *Electrochem. Commun.*, **6**, 1080–1084.
154. Solla-Gullón, J., Vidal-Iglesias, F.J., López-Cudero, A., Garnier, E., Feliu, J.M., and Aldaz, A. (2008) Shape-dependent electrocatalysis: methanol and formic acid electrooxidation on preferentially oriented Pt nanoparticles. *Phys. Chem. Chem. Phys.*, **10**, 3689–3698.
155. Grozovski, V., Solla-Gullon, J., Climent, V., Herrero, E., and Feliu, J.M. (2010) Formic acid oxidation on shape-controlled Pt nanoparticles studied by pulsed voltammetry. *J. Phys. Chem. C*, **114**, 13802–13812.
156. Solla-Gullon, J., Vidal-Iglesias, F.J., and Feliu, J.M. (2011) Shape dependent electrocatalysis. *Annu. Rep. Prog. Chem. Sect. C: Phys. Chem.*, **107**, 263–297.
157. Martinez-Rodriguez, R.A., Vidal-Iglesias, F.J., Solla-Gullon, J., Cabrera, C.R., and Feliu, J.M. (2014) Synthesis of Pt nanoparticles in water-in-oil microemulsion: effect of HCl on their surface structure. *J. Am. Chem. Soc.*, **136**, 1280–1283.
158. Sebastian, P., Sandoval, A.P., Climent, V., and Feliu, J.M. (2015) Study of the interface Pt(111)/Emmim NTf2 using laser-induced temperature jump experiments. *Electrochem. Commun.*, **55**, 39–42.
159. Sandoval, A.P., Feliu, J.M., Torresi, R.M., and Suarez-Herrera, M.F. (2014) Electrochemical properties of poly(3,4-ethylenedioxythiophene) grown on Pt(111) in imidazolium ionic liquids. *RSC Adv.*, **4**, 3383–3391.
160. Sandoval, A.P., Suarez-Herrera, M.F., and Feliu, J.M. (2014) Hydrogen redox reactions in 1-ethyl-2,3-dimethylimidazolium bis(trifluoromethylsulfonyl)imide on platinum single crystal electrodes. *Electrochem. Commun.*, **46**, 84–86.